DARTS: Multi-year database of AI-detected retrogressive thaw slumps in the circum-arctic permafrost region

Ingmar Nitze[*,1], Konrad Heidler[2], Nina Nesterova[1,3], Jonas Küpper[4], Emma Schütt[1,3], Tobias Hölzer[1,3], Sophia Barth[1,3], Mark J. Lara[5,6], Anna K. Liljedahl[7] & Guido Grosse[1,3]

1 Permafrost Research Section, Alfred Wegener Institute Helmholtz Centre for Polar and Marine Research, 14473 Potsdam, Germany

2 Chair of Data Science in Earth Observation (SiPEO), Department of Aerospace and Geodesy, TUM School of Engineering and Design, Technical University of Munich (TUM), 80333 Munich, Germany

3 Institute of Geosciences, University of Potsdam, 14469 Potsdam, Germany

4 Computing and Data Centre, Alfred Wegener Institute Helmholtz Centre for Polar and Marine Research, 27570 Bremerhaven, Germany

5 Department of Plant Biology, University of Illinois at Urbana-Champaign, 61801 Urbana, Illinois, USA

6 Department of Geography, University of Illinois at Urbana-Champaign, 61801 Urbana, Illinois, USA

7 Woodwell Climate Research Center, 02540 Falmouth, Massachusetts, USA

* Corresponding author: ingmar.nitze@awi.de

Dataset: https://doi.org/10.18739/A2RR1PP44

Ingmar Nitze, Konrad Heidler, Nina Nesterova, Jonas Küpper, Emma Schütt, Tobias Hölzer, Sophia Barth, Mark J Lara, Anna Liljedahl, & Guido Grosse. (2024). DARTS: Multi-year database of AI detected retrogressive thaw slumps (RTS) and active layer detachment slides (ALD) in hotspots of the circum-arctic permafrost region - v1. Arctic Data Center. doi:10.18739/A2RR1PP44.

Keywords: Permafrost, retrogressive thaw slumps, dataset, pan-arctic, deep learning, artificial intelligence, thermokarst, active layer detachment slides, hillslope thermokarst

Preprint Statement: This manuscript is a non peer-reviewed preprint submitted to EarthArXiv. This manuscript was submitted to Scientific Data.

Abstract

Retrogressive Thaw Slumps (RTS) and Active Layer Detachment Slides (ALD) are widespread thermal mass-wasting hillslope failures triggered by thawing permafrost. Despite increasing rates of these failures, knowledge about their pan-arctic spatial and temporal distribution remains limited. We present the Database of AI-detected Arctic RTS and ALD footprints (DARTS), the largest hillslope thermokarst database with over 43,000 individual features. which spans approximately 1.6 million km² for 2018 to 2023 and at least annual coverage in 2021 to 2023 for a ~900,000 km² region. DARTS is freely available in two processing levels: sub-annual and annually aggregated polygon footprints. The database was created with a fully automated workflow that leverages deep learning-based segmentation of PlanetScope multi-spectral imagery (3-5m spatial resolution) with minimum annual coverage. We validated DARTS using different datasets, achieving F1 scores ranging from 0 to 0.519, with more accurate results in RTS-rich areas. The DARTS database will be valuable for mapping, quantifying, and understanding hillslope thermokarst distribution and change over time across the circum-arctic permafrost region.

Introduction

As permafrost warms and thaws (Biskaborn et al., 2019; Smith et al., 2022), it is critical to understand the processes driving different modes of gradual versus abrupt thaw and how they are influenced by Arctic change (Turetsky et al., 2019). Retrogressive Thaw Slumps (RTS) and Active Layer Detachment Slides (ALD) are among the most striking forms of rapid degradation in permafrost regions (Kokelj et al., 2021; Nesterova et al., 2024). These mass wasting features, often referred to as hillslope thermokarst, form in permafrost terrain with steeper elevation gradients, such as hillslopes or coastlines, which enable thaw, meltwater runoff, and the downslope movement of thawed material.

Local to regional scale studies have identified an increase in the abundance and frequency of RTS and ALD since the 1980s (Kokelj et al., 2015; Lantz & Kokelj, 2008; Lewkowicz, 2024b; Lewkowicz & Way, 2019; Liu et al., 2024; Ward Jones et al., 2019). However, their spatial distribution across the vast circum-arctic region, particularly in Siberia, remains poorly quantified, with only a few publicly available regional datasets(Lewkowicz, 2024b; Nesterova et al., 2021; Xia et al., 2024). This creates a significant knowledge gap regarding their influence on regional and global carbon dynamics, ecosystems, and climate systems. The remote locations, dynamic nature, and relatively small size of RTS and ALD make them challenging to monitor and quantify using publicly available satellite imagery, such as Landsat's 30-meter resolution and Sentinel-2's 10-meter resolution.

Retrogressive thaw slumps, forming only in very ice-rich permafrost, consist of distinct morphological components, including a headwall, scar zone, and debris tongue that can range in size from a few square meters up to around one km² (Kizyakov et al., 2024). They are typically found in regions with ice-cored moraines or ice-rich yedoma permafrost and require sloped terrain to re/initiate, which is often found along shorelines of the sea, lakes or rivers. While these features often exhibit spatial clustering due to specific formation conditions, they remain relatively sparse across the landscape.

These permafrost thaw features are triggered by the thawing and collapse of ice-rich ground, which propagates upslope through ice ablation (Burn & Lewkowicz, 1990). As a geohazard on local to regional scales, RTS contribute to soil and carbon mobilization and significantly impact local hydrology (Kokelj et al., 2021) (Kokelj et al, 2021). They exhibit temporal variability and often demonstrate polycyclic dynamics (i.e., recurring over time) (Kerfoot, 1969; Mackay, 1966), influenced by climate, extreme weather variability, and local geomorphological conditions. Active layer detachment slides (ALD) are shallow permafrost landslides at the base of the active layer (the seasonally thawed layer) (Kokelj & Jorgenson, 2013; Leibman et al., 2014; Lewkowicz, 2007). These slides often initiate further thaw, leading to the formation of RTS (Lacelle et al., 2010; Lewkowicz & Harris, 2005; Swanson, 2021). From down-looking remote sensing imagery, RTS and ALD appear highly similar due to the typically dark grey color of bare

disturbed ground, making them difficult to distinguish from RTS, landslides or bare ground in general. Figure 1 shows examples of RTS and ALD.

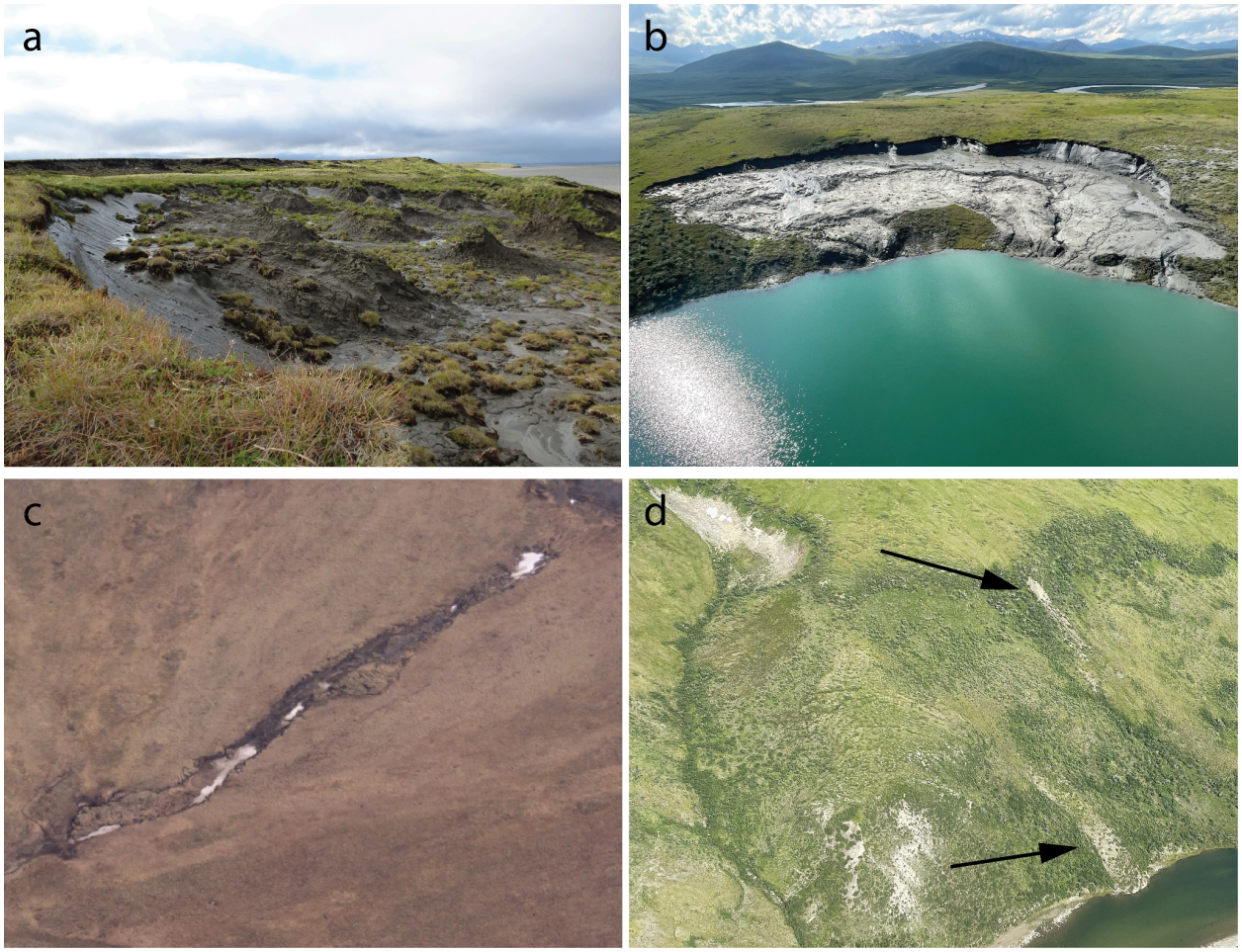

Figure 1: Examples of retrogressive thaw slumps (RTS) and active layer detachment slides. a) Ground view of a coastal elongated/terraced RTS typical for Yedoma ice-rich permafrost on the Bykovsky Peninsula in the Lena Delta Region, northeast Siberia. Photo: I. Nitze. b) RTS along a lake shore with a notable headwall and scar zone in the Brooks Range in northern Alaska. Photo: M.J. Lara. c) Active layer detachment slide in the Brooks Range foothills in northern Alaska. Photo G.Grosse. d) Active layer detachment slides (marked by arrow) in a previously disturbed hillslope in the Brooks Range in northern Alaska. Photo M.J.Lara.

Historically, research on the spatial distribution and temporal dynamics of retrogressive thaw slumps (RTS) has concentrated on regions in Northwest Canada (Kokelj et al., 2017; Lantuit & Pollard, 2008; Mackay, 1966) and Northwest Siberia (Babkina et al., 2019; Leibman et al., 2014). However, with improved remote sensing data availability—particularly from high-resolution satellite, airborne, and uncrewed aerial vehicle (UAV) imagery - mapping and monitoring RTS and ALD over large regions has become more feasible. Many mapping initiatives are still manually or semi-automatically driven e.g. (Kokelj et al., 2023; Lewkowicz, 2024b) as RTS and ALD can be challenging to detect and delineate properly even for experts (Nitze, Van Der Sluijs, et al., 2024). These initiatives have enhanced our understanding of RTS and hillslope thermokarst dynamics, particularly in NW Canada (Kokelj et al., 2021, 2023) and provide potential data sources for training more automated detection approaches. In Siberia,

ongoing efforts to map and quantify RTS and hillslope thermokarst near the Yamal and Gydan Peninsulas (Nesterova et al., 2021) and further sites sites such as Kolguev Island, Novaya Zemlya or Taymyr among others (Barth et al., in review) have also been the focus of similar mapping initiatives. Such studies focused on local to regional scales typically use manual mapping methods, which are not feasible at circumpolar scales.

Thus, more automated processing techniques need to be applied to properly quantify RTS dynamics across the northern circumpolar permafrost region, leveraging advancements in computational power and computer vision technology such as deep learning. Significant advances have been made in this field, with RTS mapping studies across several regions and scales employing different methodologies and achieving varying accuracies. Various approaches and data sources have been tested.

On one hand, differential elevation data have been used to map elevation and volumetric changes. This includes local studies using photogrammetric methods with high resolution aerial imagery in the Noatak Valley in northern Alaska (Swanson & Nolan, 2018) as well as regional mapping and change analysis based on differential TanDEM-X digital elevation models (DEMs) on a regional scale in northern Siberia (Bernhard et al., 2020, 2022). A pan-arctic analysis based on differential ArcticDEM was carried out by (Huang et al., 2023), who found 2,494 active RTS across the Arctic; however, this likely underestimates RTS abundance. In a very similar approach, also pan-arctic approach, (Dai et al., 2024) analyzed volumetric changes of different processes, including some RTS.

The second approach involves using deep learning segmentation or object detection techniques on predominantly optical satellite imagery. Over the last decade or so, machine learning and deep learning (DL) have become increasingly common methods for detecting and segmenting anthropogenic and natural objects in remote sensing imagery. On the Qinghai-Tibetan Plateau, recent advances have been made to map RTS in detail with a hybrid semi-automated approach, producing high quality RTS footprints since 2016 (Xia et al., 2024).

For a large region in northeastern Siberia, (Runge et al., 2022) used time series analysis with LandTrendr on Landsat data to map RTS-like disturbances. (Nitze et al., 2018) employed a similar approach on Landsat trend data to map RTS, but both studies relied on Landsat with a limited spatial resolution of 30 m, which is too coarse for many RTS. More recent studies focused on image segmentation deep learning techniques on higher-resolution data with 3–5 m spatial resolution, such as PlanetScope, or very-high-resolution (VHR) Maxar imagery with 1 m or better spatial resolution. However, these sources are commercial datasets and thus costly or only accessible with specific research licenses, which limits their accessibility.

An important aspect in recent research has also been the accuracy of semantic or instance segmentation and feature detection with DL. Precision and recall as well as their harmonic mean F1 score, and Intersection-over-Union (IoU) are typically used as main segmentation and detection metrics, with IoU being mostly used for segmentation tasks and validation. With VHR satellite imagery, (Witharana et al., 2022) tested the applicability of a U-Net deep learning model for segmenting RTS footprints in two sites in the Canadian high Arctic using a fully automated workflow. They achieved F1 scores of 0.75-0.85 on a held-out test set of their training and validation data. Using a similar methodology, (Yang et al., 2023) employed a U-Net3+ convolutional neural network based on 4-meter Maxar base maps and ArcticDEM elevation data to test an automated approach focused on NW Siberia but also evaluating other sites across the Arctic. They achieved F1 scores of 0.71-0.74, using the same validation scheme. An intense test and parametrization of RTS segmentation has been carried out by (Nitze et al., 2021). They used PlanetScope imagery, ArcticDEM-derived elevation and slope data, as well as Landsat trend information, and tested various deep learning architectures while performing regional cross-validation to assess spatial transferability and scalability. In this study, which used regional cross-validation to test spatial transferability, the models achieved F1 accuracies of 0.25-0.73. Using PlanetScope imagery on the QTP, (Huang et al., 2020) achieved F1 scores of even 0.85, though in a limited region of 5,500 km². All of the

presented studies have in common that they used internal validation, often using the same or similar regions, but without external datasets for comparison. The validation may show good internal consistency, but spatial scaling and transferability might pose different challenges. The lack of proper training and validation data from multiple sources might help to benchmark data products and to upscale processing significantly. First efforts have been taken to provide RTS labels from a wide variety of geographies and RTS types, such as (Nitze, 2024) or the ARTS database (Yang et al., 2024). However, as shown in a RTS mapping experiment with multiple contributors of different expertise levels, expert-drawn labels for RTS can vary strongly based on prior expertise, scientific background, and scientific goal of the mapping (Nitze, Van Der Sluijs, et al., 2024), which implies that creating proper RTS training and validation datasets is challenging.

To overcome the issue of limited training sets, (Heidler et al., 2024) applied a novel semi-supervised approach called PixelDINO, where the model creates and iteratively updates and thus enhances labels internally. This technique was tested in pan-arctic limited samples on Sentinel-2 data and out-performed supervised approaches by a considerable margin.

Recently the image based deep-learning technology shifted towards vision transformers and very large multi-purpose foundation models, which are potentially more accurate and can also take additional information such as spatial location (Klemmer et al., 2024) or temporal information into account (Cong et al., 2022; Jakubik et al., 2023). However, in permafrost-related research the usage of these techniques is in its infancy.

In this study, we build upon the work of (Nitze et al., 2021) to develop a blueprint for a pan-Arctic RTS monitoring system that incorporates regular updates using high-resolution remote sensing, Unet++ Convolutional Neural Networks, and targeted data and image post-processing. Here we present the first version (v1) of our automated RTS and ALD detection dataset DARTS, which covers hillslope thermokarst hotspots around the pan-arctic permafrost region. In its first version, it covers a total area of ~1.64 million square kilometers with at least one coverage between 2018 and 2023. Our core region encompasses an area of around 900,000 km² and provides at least annual coverage between 2021 and 2023.

We here provide a thorough overview of our dataset with used data and methods, as well as validation, the description of possible use cases, and current limitations. Furthermore we present basic statistics of RTS abundance and data coverage. The methodology and dataset will be actively maintained and improved in accuracy and spatio-temporal coverage and we envision regular releases in the foreseeable future. This dataset, the first of its kind, could be used for several purposes, such as mapping and quantifying RTS and ALD dynamics across the pan-arctic, permafrost vulnerability assessments, or for parameterizing landscape and carbon dynamics models.

Data and Methods

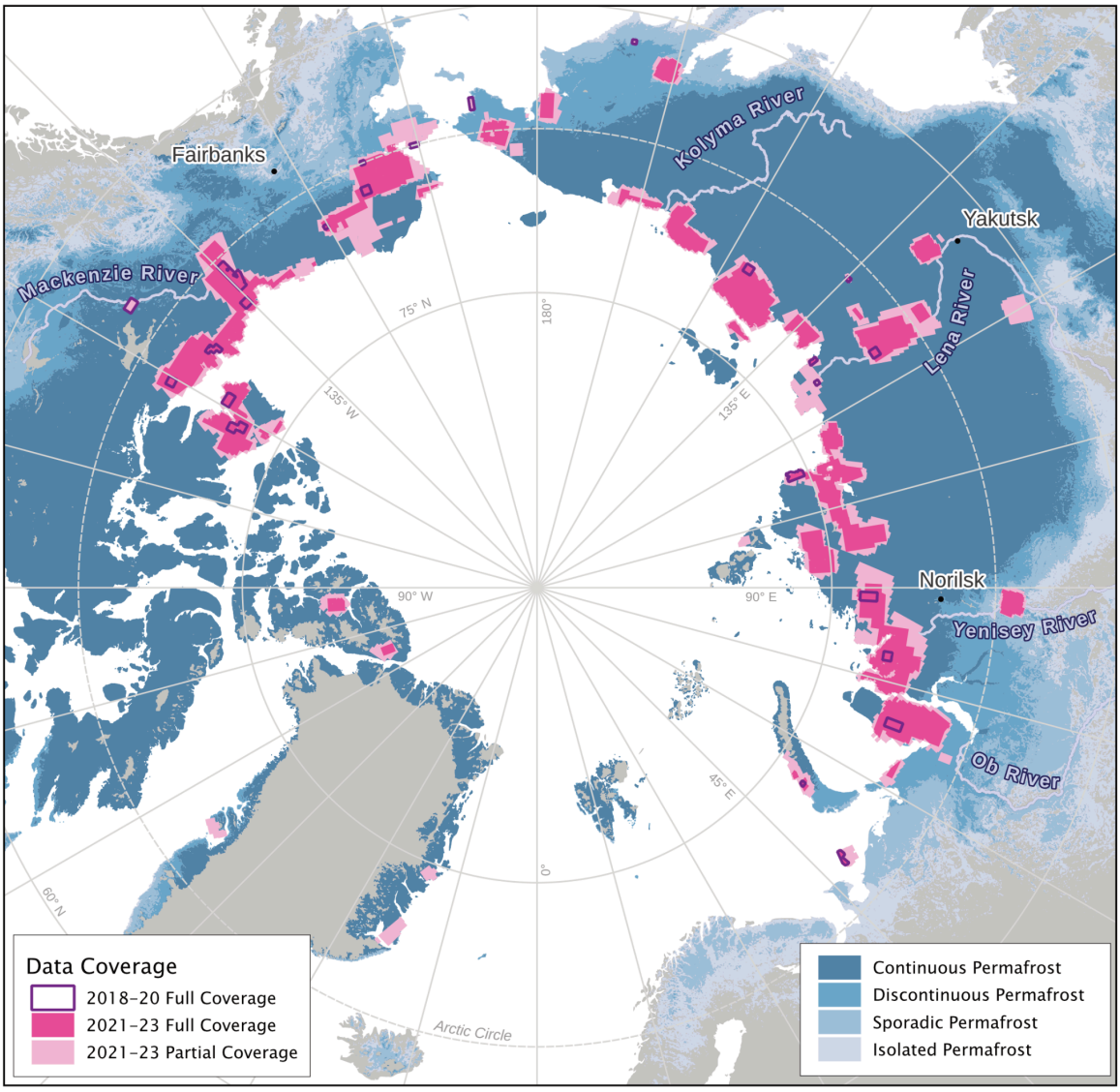

Figure 2: Spatial distribution of DARTS data data coverage for core regions in 2018-2023 (dark purple outlines, annual coverage 2021-2023 (dark pink), and partial coverage (at least once) 2021-2023 in light pink. Permafrost extent is shown in blue shades (Obu et al., 2018).

Data

We utilized PlanetScope multi-spectral optical satellite imagery (Planet Team, 2017) as our primary data source for extracting the RTS footprints. In addition, we incorporated relative elevation and slope data derived from the ArcticDEM mosaic in Version 3.1 (Porter et al., 2018) the Landsat Trends dataset (Nitze, Lübker, et al., 2024; Nitze & Grosse, 2016). Please find a detailed description below. Our data setup closely follows the methodology outlined in (Nitze et al., 2021).

PlanetScope imagery comprises four spectral bands: Blue, Green, Red, and Near-Infrared, with a ground sampling distance (GSD) ranging from 3.7 to 4.1 meters. The satellites offer a high revisit frequency of less than one day, particularly in high-latitude regions, supported by a fleet of over 180 satellites. Since its launch in 2016, data acquisition frequency has improved, resulting in greater image availability in more recent years.

We employed two data products from PlanetScope: PlanetScope Scenes (PSScene), which are individual scenes at 3-meter spatial resolution following the original acquisition swaths, and PlanetScopeOrthoTile (PSOrthoTile), which are aggregated data on a gridded footprint with a resolution of 3.125 meters. However, as of 2024, PSOrthoTile products have been discontinued. Initially, we favored PSOrthoTiles for their advantages in data management and organization but have recently transitioned to using PSScene. This mixed input structure is reflected in our output products and metadata.

We downloaded data covering a substantial and representative portion of RTS hotspots across the Arctic from 2021 to 2023 (Figure 2). We began with known hotspot regions based on relevant publications and ongoing RTS research, including Northwest Canada (Kokelj et al., 2023; Lewkowicz, 2024b), the Yamal and Gydan Peninsulas in Western Siberia (Leibman et al., 2014; Nesterova et al., 2021), and the Taymyr Peninsula in Northern Siberia (Bernhard et al., 2020, 2022). We then expanded our geographic scope by identifying additional regions of potential RTS activity using the Landsat Trends dataset, which visualizes land surface changes over two decades (Nitze, Lübker, et al., 2024). This allowed us to locate active hillslope thermokarst regions across the Arctic, such as Novaya Zemlya, NW Alaska, and various areas in NE Siberia with RTS in Yedoma ice-rich permafrost, which are less documented in the RTS literature. Data for 2021 and 2022 are predominantly from PSOrthoTile, while the 2023 data are mostly PSScene. Gap filling for all years was done with PSScene data.

For selected hotspot regions, such as parts of the Peel Plateau, Banks Island, or East Taymyr, among others, we acquired additional data from 2018-2020, partially at a higher frequency, to extend the time-series for these particularly research-intensive areas, which encompass an area of around 65,000 km² (see Figure 2). Our data coverage encompasses approximately 1.64 million km² with at least one coverage between 2018 and 2023. Our core region with at least annual coverage between 2021 and 2023 encompasses around 900,000 km². Coverage of individual years (2021-2023) typically covers larger areas, but may not have observations during other years in smaller areas. Table 1 lists detailed numbers of data coverage.

Table 1: Number and area of input scenes and detected RTS/ALD features for both processing levels; Level 1: images scenes and Level 2: annually aggregated data.

	Data Coverage			**RTS/ALD Features**			
	Level 1		**Level 2**	**Level 1**		**Level 2**	
Year	**Area [km^2]**	**Images [#]**	**Area [km^2]**	**Area [km^2]**	**Features [#]**	**Area [km^2]**	**Features [#]**
2018	121,468	350	65,671	43.82	5,083	32.42	3,539
2019	121,673	364	66,324	65.05	5,999	46.74	3,988
2020	154,008	439	70,959	81.26	7,417	53.62	4,335
2021	2,468,881	5,927	1,197,632	223.79	29,237	146.41	19,733
2022	2,586,401	5,858	1,098,728	329.41	35,176	159.44	19,947
2023	2,898,801	4,231	1,386,600	266.10	36,537	153.38	22,966
SUM	**8.351,232**	**17,169**	**3,885,914**	**1009.43**	**119,449**	**592.01**	**74,508**
Union (2018-2023)	—	—	1,636,692	—	—	286.98	43,572

Intersect (2021-2023)	—	—	898,212	—	—	261.71	35,349

We aimed to capture imagery during the peak summer season (July 1 to August 31). When cloud-free data was unavailable, we extended our search into September, which was necessary for far northern sites like the Canadian Archipelago, where coastal fog is less prevalent in late summer. However, low sun angles, large cast shadows, and occasional snow limited usability in September. For data selection, we queried images with less than 20% cloud cover and manually selected data using the QGIS Planet plugin, which offers effective preview and ordering capabilities. Due to limitations in accessible data quotas and insufficient metadata quality, particularly regarding cloud cover estimates, we conducted visual inspections to ensure efficient data usage. For each PlanetScope image we calculated the Normalized Difference Vegetation Index (NDVI) (Huete et al., 2002) as a simple feature engineering step, to enhance the vegetation information.

In addition to the Planet input data, we incorporated auxiliary data to provide geomorphological context and basic temporal information, as the model is temporally agnostic, thus does not take time-series information into account in the current version.

We added derived data from ArctciDEM version 3.1. We calculated a relative elevation, calculating the relative position of the pixel location within a circular kernel with a diameter of 100m. We chose the relative elevation to obtain the relative position in the landscape and to avoid absolute elevation, which are highly variable for RTS. Furthermore we calculated the slope values. We preprocessed the DEM derived data in Google Earthengine (GEE) and downloaded them to local storage and finally created virtual raster tile (*vrt*) mosaics.

Additionally, we downloaded the Landsat Trends layer, called (TCVIS - Tasseled Cap VISualization), which contains the slope or change rate of Tasseled Cap indices over a 20 year period, based on Landsat data and thus contains basic time-series information of land surface changes. This dataset type has been described in (Nitze & Grosse, 2016) and has been used for identifying rapid land surface dynamics in the permafrost regions such as lake changes, wildfires or RTS (Nitze et al., 2017, 2018; Runge et al., 2022). This dataset is available as a public asset in GEE (“users/ingmarnitze/TCTrend_SR_2000-2019_TCVIS”) and covers the period from 2000 to 2019. A more detailed description of auxiliary data is available in (Nitze et al., 2021) . The final input dataset comprises five types of information (satellite imagery, NDVI, relative elevation, slope, and Landsat trends) with a total of ten input layers/bands, readily available for the deep learning models (Table 2) .

For our DARTS dataset we used 17,169 images (PSScenes and PSOrthoTiles) between 2018 and 2023 (Table 1). They cover a total gross area of ~8.35M km². The majority of images (16,016) fall into our key period between 2021 and 2023 and have a gross coverage of ~7.95 million km² or around 880 billion pixels of raw imagery. For this key period we used 4231 to 5927 images annually, covering a net area (without overlap) of ~1.1 to 1.39 M km² each year.

Table 2: Overview of input datasets with number of bands, derived dataset if specifically processed, if it was used for the two AI models and the citation of the data source.

Dataset name	nBands	Derived from	tcvis	notcvis	Data source and citation
PlanetScope	4	—	Yes	Yes	Planet Scope data: (Planet Team, 2017)
NDVI	1	PlanetScope	Yes	Yes	Calculated from PlanetScope

Relative elevation	1	ArcticDEM	Yes	Yes	ArcticDEM: (Porter et al., 2018)
Slope	1	ArcticDEM	Yes	Yes	See above
TCVIS	3	—	Yes	No	Methodology: Nitze et al (2016)

Methods

Our deep learning based dataset processing can be broadly divided into training and inference workflows. These workflows share common steps such as data preprocessing but primarily consist of separate steps. We describe the specific workflows in detail below. The Python code for the full data processing workflow is available on GitHub (https://github.com/initze/thaw-slump-segmentation). We utilized PyTorch (Paszke et al., 2019) together with the Segmentation Models package for the PyTorch library (Iakubovskii, 2019), for the deep learning part of our pipeline. For the data processing part we used common Python Geo-Libraries. This codebase is actively maintained and undergoes continuous improvement. We created the DARTS dataset using our custom thaw-slump-segmentation python package, which has all available functionalities (Nitze, Heidler, et al., 2024). The schematic workflow for our processing pipeline is shown in Figure 3.

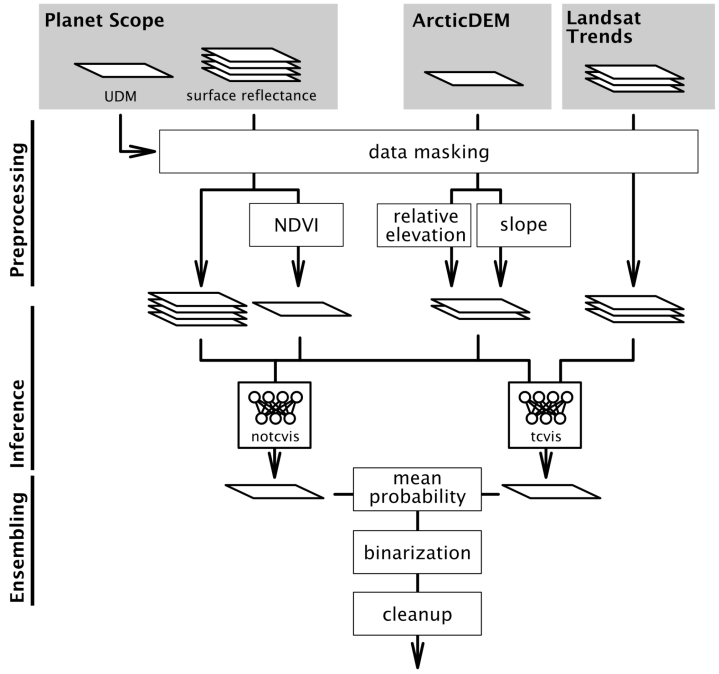

Figure 3: Simplified workflow of RTS dataset inference pipeline with preprocessing, inference, and ensembling stages.

Data Preprocessing

Deep Learning Model Setup

Overview

Our model training process consisted of several steps, which we developed iteratively. While the training steps are fundamentally based on (Nitze et al., 2021), they underwent several further iterations and improvements. The general steps of our pipeline consist of (1) label creation, (2) model training, and (3) model ensembling and data cleaning.

Label Creation

We followed the labeling procedures outlined in (Nitze et al., 2021). The labeling was primarily performed on PlanetScope imagery, with support from auxiliary datasets such as Landsat Trends (Nitze, Lübker, et al., 2024; Nitze & Grosse, 2016) to distinguish retrogressive thaw slumps (RTS) and active layer detachments (ALD) from stable bare ground like rock outcrops. Furthermore, we used additional very high-resolution datasets such as the ESRI and Google Satellite basemaps.

We employed an iterative approach for labeling, training, validation, and subsequent inference. After each label iteration, we trained the model(s) and ran inference on a larger region. Following visual inspection, we repeated this pipeline and created new labels in areas where the previous model performed poorly. We completed six iterations in total, which is reflected in the available training labels. The early iterations consisted of predominantly positive labels, where only regions with active RTS were labeled. In iterations 005 and 006, more negative samples in regions without RTS were added. The necessity for more negative labels was driven by a large rate of false positives, which we tried to overcome by adding more regions without the positive class. Strategically we aimed to cover the large variety of permafrost landscapes, where RTS and ALD are or could be present and also to cover the general variability of the pan-arctic permafrost region. The final training database contains 3749 features, acquired across 198 image scenes from between July 2018 and August 2022 (see Supplementary Table S1).

The labels are polygons (Geopackage format) representing the bare soil or scar zone of RTS and ALD. We chose to label only the active parts without vegetation, as this specific setup is more feasible when using optical satellite images compared to the entire morphological feature. For the labeling process, we predominantly worked in a team of two with internal guidelines and mutual feedback. While having guidelines is highly recommended and considered best practice, achieving complete label consistency remains challenging (Nitze et al., 2024). Multiple visual examples of labeled data are shown in (Nitze et al., 2021).

Training labels are freely available on Zenodo (Nitze, 2024), https://zenodo.org/doi/10.5281/zenodo.12706220) and GitHub (https://github.com/initze/ML_training_labels) as polygon vectors in *Geopackage* format. Footprints of the labeled images are available in the same location. Our training dataset is also part of the ARTS RTS database (Yang et al., 2024) (https://doi.org/10.18739/A2PK0738B). Locations of labeled regions are shown in Figure 4. Details about the training dataset are shown in Supplementary Table S1.

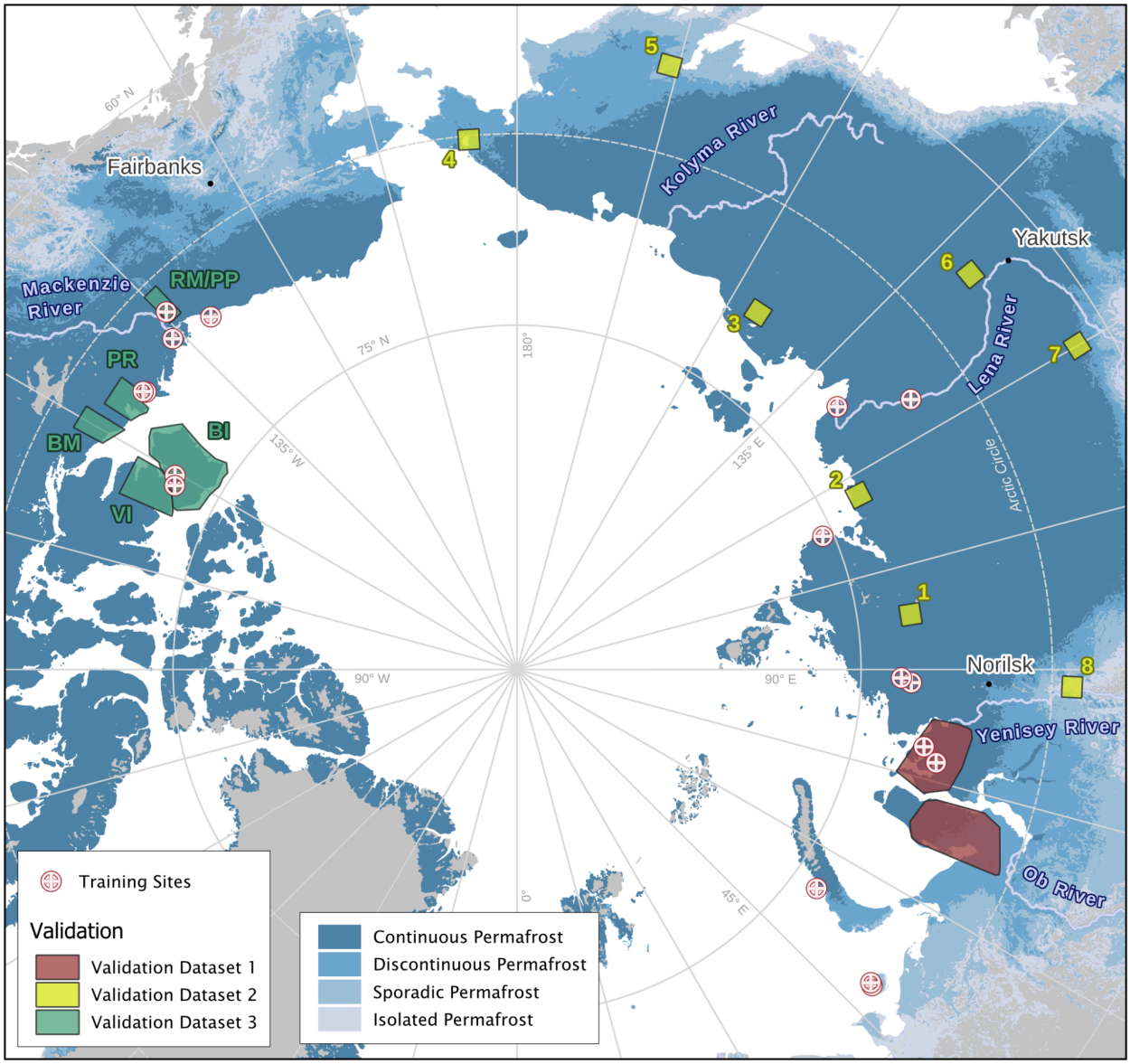

Figure 4: Location of sites where training data was gathered as well as the 3 dataset validation regions of internal validation in northwest Siberia (Validation Dataset 1), various regions in Siberia (Validation Dataset 2) and the external dataset by (Lewkowicz, 2024a) in northwest Canada (Validation Dataset 3). Training time validation was run on a subset of the training dataset.

Model Training

Our model training was founded on the work of (Nitze et al., 2021), who performed exhaustive testing of architecture and backbone configurations. Their results showed that Unet++ (Zhou et al., 2018) with a resnet34 backbone performed best. The models from Nitze et al were the first iteration. We ran in total six training cycles (iterations), as described above.

After the first iteration, we conducted further tuning steps for model depth learning rate scheduling, tile size, and input band combinations. Our tests included fixed, gamma, and step learning rate schedules. An exponential learning scheduler (*ExponentialLR*) with a gamma of 0.9 and an initial learning rate of 1e-3

proved most effective for our iterative training with pre-trained weights on pretrained models, in iterations 2 to 6. We evaluated tile sizes of 128, 256, 512, 1024, and 2048 pixels. A tile size of 1024 pixels (~3 km) outperformed smaller sizes while remaining more favorable for avoiding GPU memory issues compared to larger tile sizes. We furthermore tested model depths of 2 to 6, where a depth of 3 provided reasonably good results, while keeping the physical model size manageable to fit into GPU memory. We also tested different loss functions, and focal loss provided the best results for our models.

We applied exhaustive augmentation with geometric augmentations, such as *HorizontalFlip*, *VerticalFlip*, and *RandomRotate90*, as well as image quality augmentations, such as *Blur*, *RandomBrightnessContrast*, *MultiplicativeNoise*, and *Cutout* with a 50 percent probability during training. For augmentation we used the *albumentations* python package (Buslaev et al., 2020) (Buslaev et al., 2020) .

We further tested different input bands. The best configurations predominantly included all data bands/channels (model *tcvis*, n bands = 10). In some instances, leaving out Landsat Trends, and keeping all other bands (model *notcvis*, n bands = 7) achieved better results. The inclusion of Landsat Trends helped to identify dynamic areas, but led to false positives in areas with strong landscape change unrelated to RTS, such as along coasts or eroding river shorelines. Both model configurations suffered from too many false positives, which were either randomly distributed or overfitted in certain similar regions (see tcvis). Both model configurations suffered from false positives close to the image edges and noData, which were typically automatically masked due to clouds. Real RTS or ALD were typically detected by both models.

For training and validation of the optimization step we used fixed training and validation sets, where the validation set consisted of three scenes in the East Taymyr region in Northern Siberia. We kept the same validation set for all iterations to keep it separate from the training set. For determining the model performance we use pixelwise IoU and F1 scores of the target class as the key performance metrics, which were implemented by the torchmetrics library (Detlefsen et al., 2022).

Model ensembling and creation

Due to the high proportion of false positives, we decided to create a model ensemble where we fused the output probabilities by calculating the mean probability between both model outputs. This helped to minimize more or less random noise/hallucinations. Further we binarized the probability into 1 for RTS objects and 0 for background, at a threshold of 0.5.

On the binarized datasets we deleted all detected RTS objects, which were within 10 pixels (30/31.5 m) of the image border, as the model performed badly in these regions due to typical edge effects. Additionally we removed all objects with a size smaller than 32 pixels, realizing an effective minimum mapping unit of ~300 (288-318) m². Furthermore we used the ESRI 10m Annual Land Cover (2017-2023) dataset (Karra et al., 2021) to clean objects over water surfaces. We accessed this dataset from the GEE Community Catalog (Roy et al., 2024) through Google Earthengine (GEE) and merged the *Water* and *NoData* mask of the LC map as *Water* as the noData mask was applied over sea water. We then calculated the intersection area of each RTS polygon with the water mask. All Polygons with a fraction higher than 20 % Water were discarded. This filtering helped to minimize obvious false detections over larger water bodies (see Supplementary Figure S1).

Inference / Dataset production

For inference, we developed a highly automated pipeline. Over several years, we downloaded PlanetScope data, initially in PSOrthoTile format and later in PSScene products. Data downloads were typically conducted using the Planet QGIS plugin to visually inspect image quality due to limited data quotas. This visual inspection was more effective at identifying clouds than the standard metadata,

helping to avoid data gaps. After the deprecation of the gridded PSOrthoTile products, we managed our internal PlanetScope data with a SpatioTemporal Asset Catalog (STAC), as PSScene data have highly variable data footprints.

For our study area, we processed and downloaded ArcticDEM-derived relative elevation and slope data in large batches using Google Earth Engine (GEE) and stored the data locally. The remaining data layers were processed on-the-fly during batch preprocessing. For this step, we created a pipeline that uses a single Planet image scene as the basic data unit to calculate NDVI, download Landsat Trend data from GEE, and automatically clip and resample auxiliary data sources (Landsat Trends, relative elevation, slope) to match the extent and resolution of the Planet input image. Our processing automatically detects differences between PSScene and OrthoTile images, which vary slightly in pixel size. All input layers are masked where clouds are detected using the pixel-wise usable data mask (udm2) of the input image. This processing step was parallelized to enable scaling.

Finally, all layers were stacked and tiled into 1024x1024 pixel patches. We ran inference for both deep learning models, *tcvis* and *notcvis,* which output probabilities (values between 0 and 1), binary raster predictions, and polygon vector predictions of RTS and ALD presence. After model inference on the images, we also executed the ensemble and filtering processes and updated the database with new batches of incoming images. Ultimately, we automatically generated the final product sets with properly assigned metadata and attributes, along with footprint files extracted from our internal STAC catalog.

For processing, we utilized facilities at the Alfred Wegener Institute, including a NVIDIA DGX-A100 node equipped with 8xA100 40GB GPUs. Although the inference process is computationally intensive, the largest bottleneck was data storage and management.

Validation

To evaluate the accuracy of our dataset we followed different strategies during different stages of the process. We first performed *training time validation* (see details below) during the training runs of our deep learning models and subsequently validated our final dataset. During training time we validated on the pixel level, which compares the specific overlap of feature polygons.

The second validation (*dataset validation*) included the manual confirmation of detected features in NW Siberia, comparison to manually digitized features across several sites across Siberia, and comparison to the RTS location dataset by (Lewkowicz, 2024b, 2024a). The dataset validation was carried out on the object level, thus we compared if our dataset intersected the reference dataset. Due to insufficient comparable datasets we decided to only compare on the object level.

The dataset validation was carried out in different stages thus, we have a slight variation of approaches. The validation was carried out in multiple stages, resulting in slightly varied approaches.

Training time validation

During training, we evaluated the pixel-wise accuracy of the class labels in a standard way similar to other deep-learning approaches. However, this validation was carried out on the initial deep learning and only provides accuracy estimates of the initial DL model *tcvis* and *notcvis* before ensembling and cleaning. We automatically retrieved standard metrics, precision, recall, F1, and Intersection over Union (IoU).

Dataset validation

Dataset Validation 1: Manual confirmation of features in NW Siberia

As the first strategy, we validated RTS and ALD polygons by manually checking each polygon from the year 2023 in the L2 dataset to determine whether it represents an RTS or ALD, or if it was falsely

detected. From our dataset, we selected a large subset of 3,668 features in NW Siberia (see Figure 4). This region covers an approximate area of 105,000 km². We utilized the available ESRI World Imagery Wayback Living Atlas and Yandex.Maps satellite basemaps. In particular cases, PlanetScope Scenes were also used. Our dataset mostly overlapped the reference basemaps temporally; however, some differences in temporal coverage may occur. This allowed us to calculate the precision of the dataset for the extensive region of the West Siberian Arctic. Each feature was manually classified as a true positive, false positive, or uncertain. With this strategy, we were able to assess the precision of our dataset. However, we could not evaluate further accuracy metrics, such as recall or F1 score, as there is currently no complete RTS ground truth dataset available for this region.

Dataset validation 2: Central and Eastern Siberia

To determine variations in model performance across a wide range of permafrost landscapes, we analyzed the model output in eight different areas of Central and Eastern Siberia: Southern Taymyr (#1), Northern Olenek (#2), Chokurdakh (#3), Iultinsky (Chukotka) (#4), Penzhina Bay (Kamchatka) (#5), Southern Verkhoyansk Range (#6), Prilenskoye Plateau (#7), and Turukhansk (#8) (see Figure 4). These areas cover a total of 80,000 km², with each site encompassing approximately 10,000 km². The sites contain RTS/ALD features to varying degrees, with some regions lacking RTS/ALD entirely. This approach also allows us to assess areas without active RTS, which are more typical across the entire permafrost region (see Figure 4).

Within each of the eight regions, we created ten randomly located squares of 100 km² each. In these subsets, we manually created a reference dataset by generously delineating RTS polygons with a 5-meter buffer based on the following basemap products: we used ESRI World Imagery for mapping RTSs, while the Arctic Landscape Explorer featuring the Landsat Trend dataset (https://alex.awi.de/), PlanetScope Scenes, Apple Maps, and Yandex Maps were utilized in ambiguous cases. The ESRI Wayback Living Atlas was consulted if none of the aforementioned maps were useful. Since we mapped only RTSs in this step, the recall values are representative of RTSs but not ALDs.

We estimated standard validation metrics: precision, recall, and the F1 score of our annual dataset (L2) in these regions. Validation was performed for each year from 2021 to 2023. Our validation was conducted at the object level, testing whether our dataset intersected with the reference dataset. Our reference dataset comprises 272 individual RTS features, of which the majority—235—are located in the four northern regions.

After standard validation procedures, we checked the false positives within the large regional subsets of 10,000 km² each for their land cover. We manually assigned each false positive to one of the following classes by visual inspection: Hills/Mountains, River, Sea, Lake, Bare Ground, Vegetation, Periglacial Landform, Other, Uncertain. This effort is intended to better understand the composition of errors to further improve the dataset for future releases.

Dataset Validation 3: Comparison with reference dataset

We compared our output data products (L2) with the published RTS point locations in five regions of NW Canada by (Lewkowicz, 2024a), namely Banks Island, NW Victoria Island, Paulatuk region, Richardson Mountains /Peel Plateau, and Bluenose Moraine, encompassing a total area of around 154,000 km². These data are evaluated in (Lewkowicz, 2024b) (see Figure 4). This dataset contains the centroids of manually detected RTS based on Landsat time-series imagery, covering the period from 1984 to 2016, compared to our annual L2 dataset from 2021 to 2023. We analyzed the spatial intersection of our dataset, which allows for the calculation of standard accuracy metrics: precision, recall, and F1 score. We analyzed accuracies for the years 2021, 2022, and 2023 of our L2 dataset.

Due to the differing temporal periods, and upslope propagation of RTS in this region, we added a buffer of 500 m to the reference dataset to minimize the effects of spatial inaccuracies and the migration of the

active parts of the RTS. However, we still anticipate a negative influence from the differences in the observation periods on the accuracy metrics.

Data Records

The DARTS dataset in version 1 is publicly available on the Arctic Data Center (arcticdata.io) available through:

https://doi.org/10.18739/A2RR1PP44 or
https://arcticdata.io/catalog/view/urn%3Auuid%3Aac45aea1-4b75-4832-84ca-489bd844a23e.

A short description of sub datasets and files is provided in Table 3.

Table 3: Overview of available geospatial dataset files with dataset type, basenames of dataset files, and short description.

Type	Basename of files	Description
Features Level 1 (2018-2023)	DARTS_NitzeEtAl_v1_features_2018-2023_level1	Footprints of RTS and ALD features, processed on individual image scenes
Features Level 2 (2018-2023)	DARTS_NitzeEtAl_v1_features_2018-2023_level2	Footprints of RTS and ALD features, maximum extent aggregated per calendar year
Coverage Level 1 (2018-2023)	DARTS_NitzeEtAl_v1_coverage_2018-2023_level1	Coverage of individual image scenes, used for the processing of DARTS Level 1 datasets
Coverage Level 2 (2018-2023)	DARTS_NitzeEtAl_v1_coverage_2018-2023_level2	Annual coverage of input images for 2018-2023
Coverage Union (2018-2023)	DARTS_NitzeEtAl_v1_coverage_2018-2023_union	Maximum coverage of the dataset with at least one coverage between 2018-2023
Coverage Intersect (2021-2023)	DARTS_NitzeEtAl_v1_coverage_2021-2023_intersect	Maximum coverage of the dataset with at least annual coverage between 2021-2023

RTS Dataset Description

The datasets are provided in OGC-compliant data formats: Geopackage and GeoParquet. Both formats consist of single files per dataset. Geopackage is a widely accepted format for various GIS software, including older versions. We recommend GeoParquet for its significantly faster performance with a high number of features and compact file size; however, compatibility issues may arise with older software versions, such as QGIS or GeoPandas. For reading GeoParquet files it is recommended to use QGIS 3.28 or higher, *geopandas* version 0.14 or higher with the *pyarrow* package for python, and sf and arrow packages for R in version 4.3 or higher. Recent versions of these applications fully support this format. All files contain polygon geometries.

The RTS and ALD datasets consist of two different processing levels and extensive geospatial coverage files, which provide information on dataset coverage and the boundaries of the input imagery.

Level 1 (L1) contains individual RTS and ALD footprints detected on individual input images. The attribute table includes the image ID, date, year, month, area in m² and ha, and information about the AI detection model for each feature.

Level 2 (L2) comprises aggregated data created from L1, representing the maximum RTS/ALD extent per calendar year. We dissolved overlapping features using the year attribute. The attribute table contains information on the number of observations, as well as the first and last observations. Due to aggregation, L2 data are typically less noisy than L1 data, which are highly dependent on image quality. We recommend using L2 data for interannual analysis. For shorter periods, L1 data provide higher spatial resolution but may be noisier.

The dataset footprints in both processing levels L1 and L2 are provided with coverage files, which provide information on image footprints for L1 and the annual maximum coverage for L2. We further provide the maximum coverage (union), which contains the area, which was at least once covered during the full observation period from 2018-2023. We also provide the region of annual coverage, or better (intersect) for our key observation period 2021-2023.

Dataset Statistics and Results

Our dataset contains 119,449 features in L1, covering a total area of 1,009.43 km², and 74,508 features in L2, with a total area of 592.01 km² across all years combined. Over the entire observation period from 2018 to 2023, we detected 43,572 unique features within an area of approximately 1.64 million km², resulting in an affected area of 0.175% of the analyzed region. In our core region, which was covered at least annually from 2021 to 2023 and spans around 898,000 km², we detected 35,349 unique features with a total area of 2,621.71 km², accounting for 0.029% of the analyzed region (see Table 1).

Figures 5 and 6 illustrate the typical expansion pattern upslope, where the headwall retreats over time in our examples from 2018-2023 and 2021-2023. Both examples show a higher number of features for L1. The lower boundaries of the scar zone may be more unstable and variable even within a single year; however, the headwall position is clearly identified. The annual aggregation in L2 removes the fuzziness observed within the scar zone but reduces the temporal resolution to annual values.

Figure 7 compares L2 data from our dataset to a high-resolution DSM from July 2023 to demonstrate the detected headwall retreat. Based on visual results, RTS and ALD were well detected despite their sparsity, intense polycyclic dynamics, and ambiguity. However, automated processing remains challenging due to specific weaknesses. Figure 8 illustrates typical or systematic false positive detections, which often occur in small rock outcrops, infrastructure, or small water bodies surrounded by vegetated surfaces.

For detailed feature description please check Supplementary Tables S2 and S3.

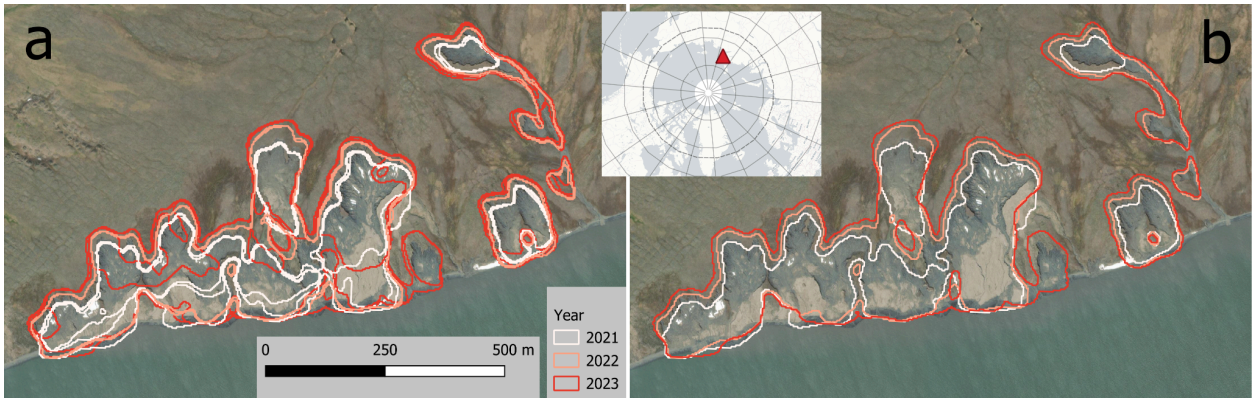

Figure 5: a) RTS Level 1 (raw dates), b) RTS Level 2 (annually aggregated), East Taymyr, N Siberia, 75.68°N, 113.16°E. Background Map: *ESRI Satellite*.

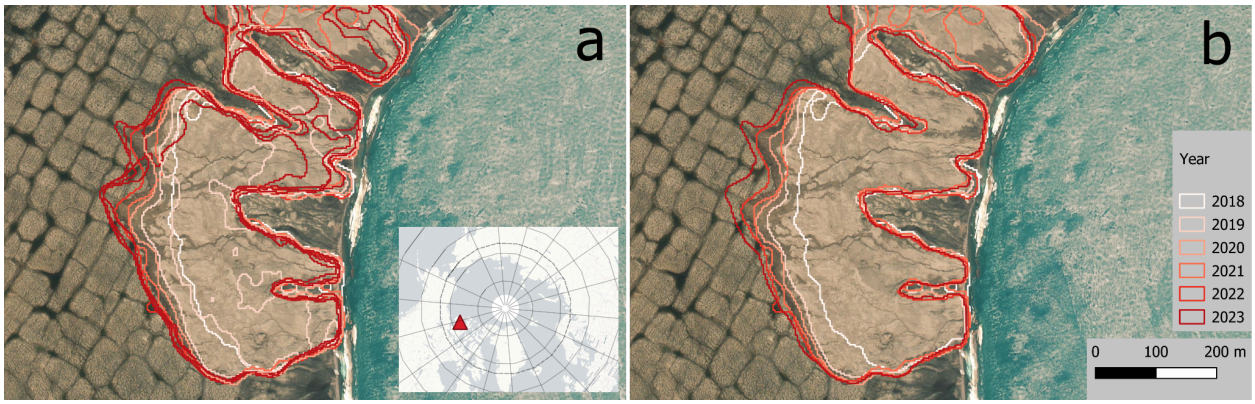

Figure 6: a) RTS Level 1 (raw dates), b) RTS Level 2 (annually aggregated). Banks Island, NW Canada, 72.97°N, 118.13°W. Background Map: *ESRI Satellite*.

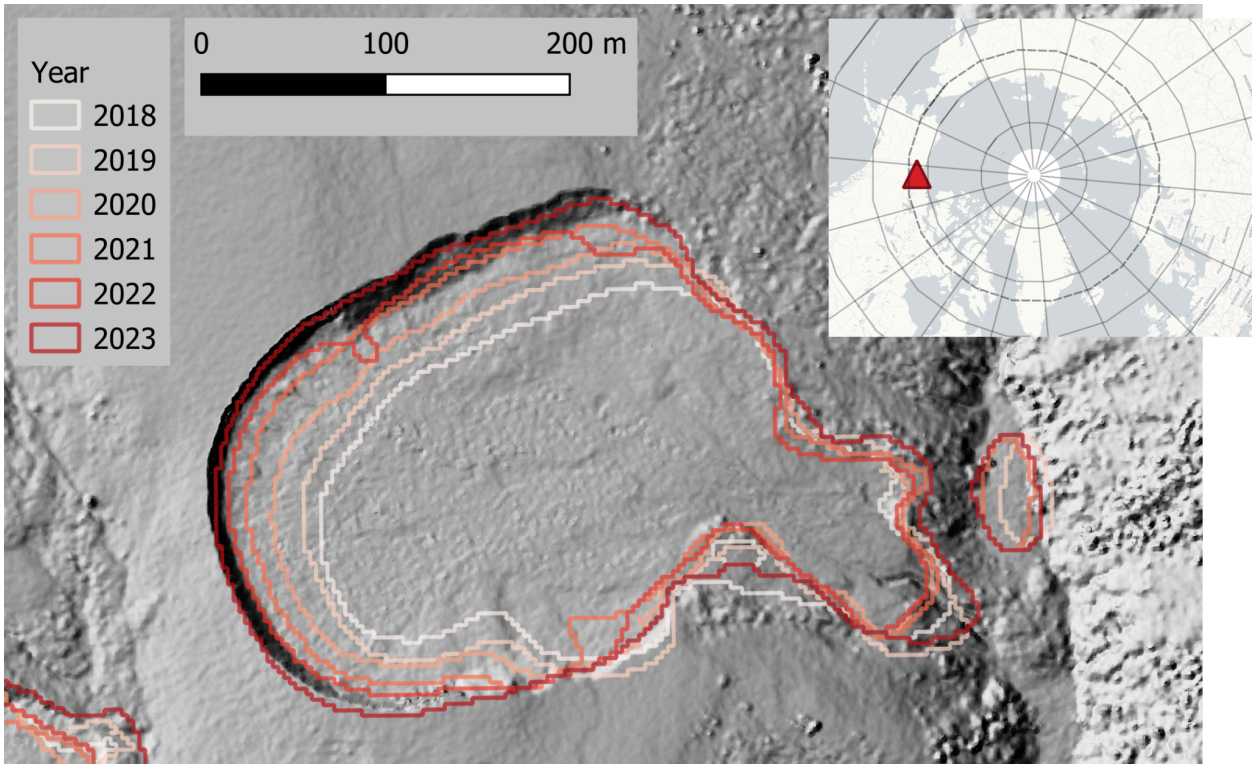

Figure 7: Examples of annual RTS time-series (Level 2 data) with notable headwall retreat, overlaid on a very high resolution hillshade on the Peel Plateau in NW Canada. 68.21°N, 136.65°W. The Hillshade layer is based on a Structure-from-Motion DSM, acquired on 2023-07-07, of the AWI PermaX 2023 aerial survey campaign.

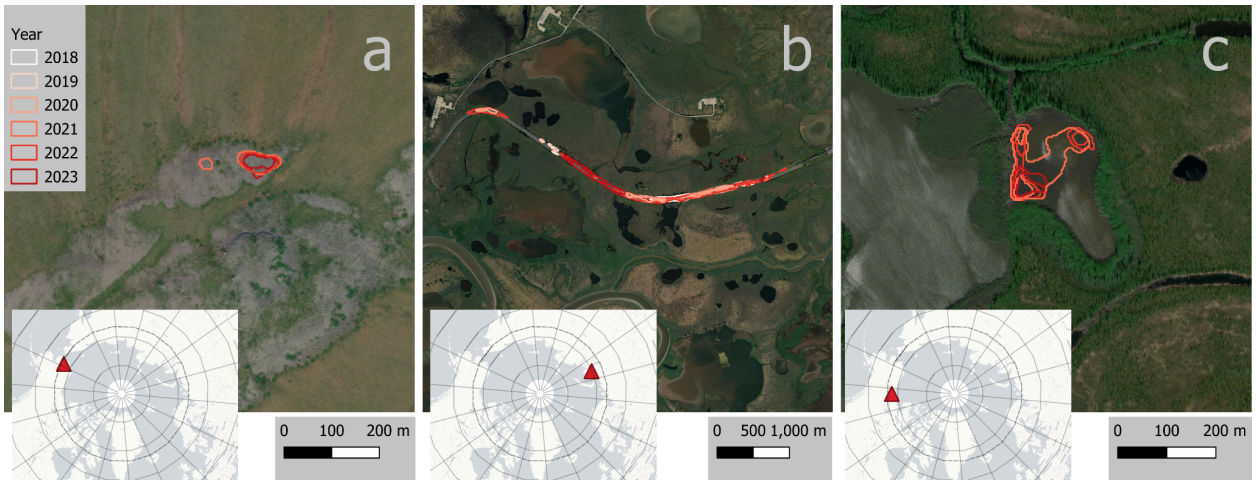

Figure 8: Examples of false detections of RTS (Level 2 data) in a) Rock outcrops, Brooks Range, Alaska, 67.41°N, 162.41°W b) linear infrastructure, Bovanenkovo, NW Siberia 70.30°N, 68.58°E, c) small water bodies surrounded by vegetation, Mackenzie Delta NW Canada, 68.13°N, 134.93°W. Background Map: *ESRI Satellite*.

Despite the challenges in automatically mapping RTS/ALD features, the regional distribution aligns well with other sources and knowledge about the spatial distributions of RTS. Figure 9 illustrates the general patterns of RTS distribution density and area across our pan-arctic research domain, showing the affected RTS area per H3 grid cell (Level 4) in percent. H3 is a hierarchical geospatial hexagonal grid system (https://h3geo.org/). The spatial patterns of RTS in NW Canada, as noted by (Kokelj et al., 2023), particularly in areas like eastern Banks Island, western Victoria Island, Peel Plateau, and Bluenose moraine, are well represented in our dataset. Additionally, the dataset reveals variability in RTS site locations. In northern Siberia, a hotspot of RTS is evident on the eastern tip of the Taymyr peninsula, with widespread occurrences across available regions, typically covering smaller areas. This basic spatial analysis highlights the general distribution patterns, aiding in the identification and analysis of the drivers of RTS presence and activity.

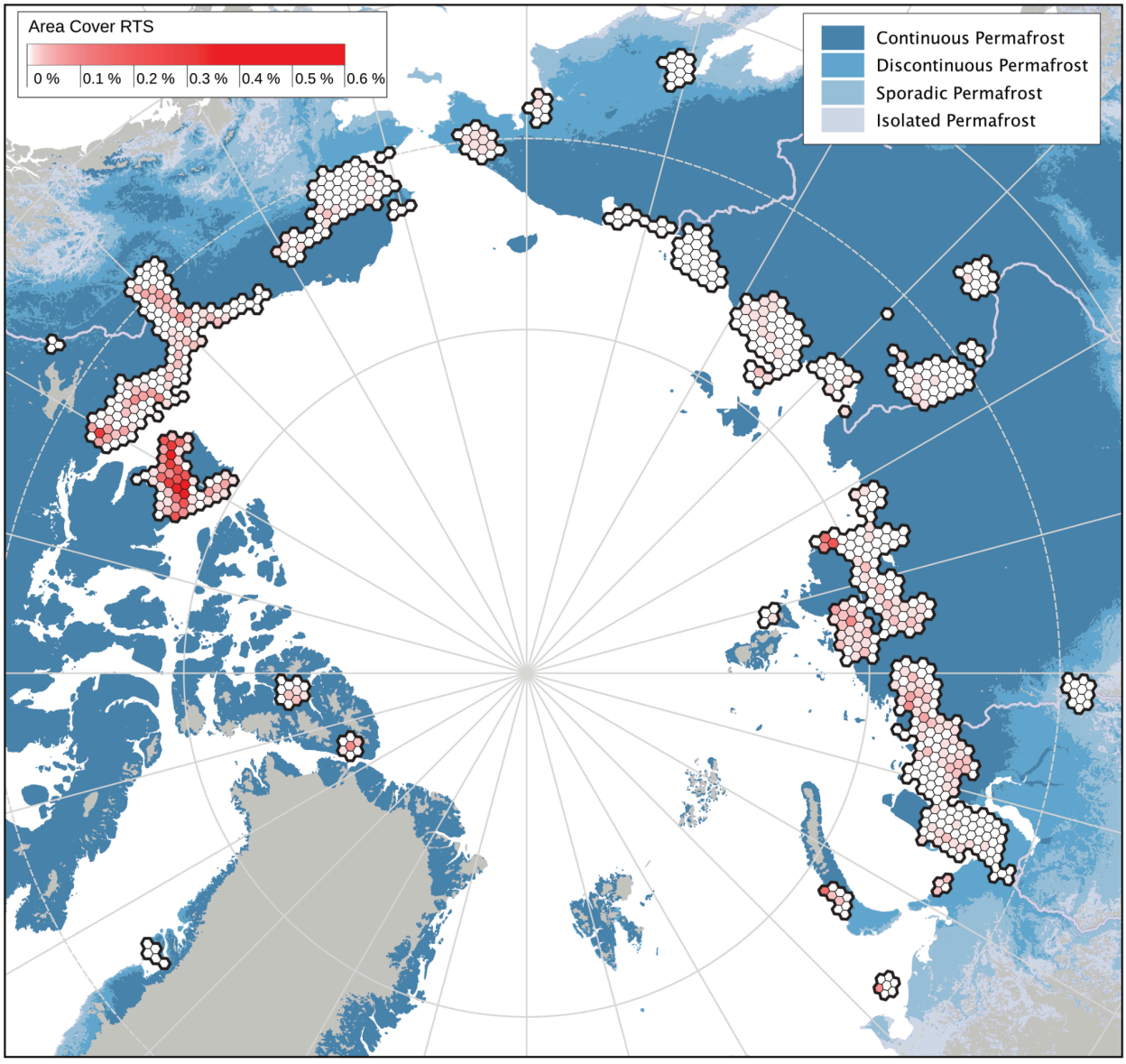

Figure 9: Affected area of RTS and ALD footprints in percent per gridcell in 2022 based on DARTS Level 2 data. Gridding is based on the H3 grid in level 4.

Technical Validation

Training Time Validation

The training time validation set achieved good accuracies, with maximum F1 scores of 0.757 and 0.797, and IoU values of 0.609 and 0.662 for the *tcvis* and *notcvis* models, respectively. The precision and recall of the best models were 0.747 and 0.767 for *tcvis*, and 0.787 and 0.806 for *notcvis*, respectively. The final models were trained and validated on pretrained RTS models from previous generations and converged at around 15 epochs(see Supplementary Figure S1)

Dataset Validation 1: Manual Confirmation NW Siberia

Of the 3,668 features present in our dataset, 2,010 were confirmed through manual evaluation. In contrast, 1,616 were identified as false positives, while 42 features remained uncertain, resulting in a precision of 0.548. Due to the absence of a ground truth dataset of this size, we cannot provide recall or F1 metrics for this set. In the second validation set, which includes eight regions across Siberia, we can provide more detailed accuracy values.

Dataset Validation 2: Validation sets Siberia and Error Types

The manual validation of our dataset revealed varying accuracies across different regions (see Table 4). Overall, the F1 score was 0.323 for 2023 over 0.419 in 2021 to 0.429 in 2022, with a precision of 0.602-0.729 and recall of 0.221-0.304. This precision/recall imbalance suggests an underestimation of features in our dataset compared to the reference datasets. However, for the reference dataset acquisition, image sources with higher spatial resolution were utilized (see Data and Methods).

The variation between regions was significant, with F1 scores ranging from 0 to 0.519±0.078. Regions with a higher abundance of features typically performed better; for example, region #1 and #3 achieved an F1 score of 0.519±0.078 and 0.510±0.079. Conversely, regions with few or no RTS (regions 5-8) exhibited low metrics due to small sample sizes, where a limited number of false positives strongly influenced regional accuracy metrics. Summarized metrics for each subregion are shown in Table 4.

A spatial analysis of 1,513 false positive (FP) features, where land cover type was manually determined, indicated a clear preference for bare ground at 64.4%. This means that nearly two-thirds of the false positives occurred on bare ground, confirming our visual inspection findings. Examples of false positives are shown in Figure 8. The next most abundant classes were lake and river at 7.87% and 7.17%, respectively, while other classes accounted for less than 5% of the false positive detections (see Table 5).

Dataset Validation 3: External Dataset Lewkowicz 2024

The comparison of our dataset to (Lewkowicz, 2024a) in five NW Canadian regions yielded F1 scores of 0.097±0.004 in the RM/PP region and up to 0.436±0.017 in Bluenose Moraine (BM), with means and standard deviations calculated over three individual years (2021 to 2023). Overall, the best performance was achieved in Bluenose Moraine, followed by Paulatak Region and Banks Island (see Table 4). F1 scores in RM/PP and Victoria Island were subpar at around 0.1.

Precision ranged from 0.056±0.007 (RM/PP) and 0.053±0.002 (VI) to 0.351±0.001 (BM). Recall was typically much higher than precision, ranging from 0.439±0.027 in PR (the lowest) to 0.687±0.0223 (the highest) in BI. The superior recall compared to precision suggests that many features in the reference dataset were successfully detected; however, an excessive number of false positives persisted.

Visual inspection also revealed that some features labeled as FP were actual true features that were either not yet present during the reference dataset's observation period (1984-2016) or fell below their detection limit. This effect of temporal mismatch is evident in the mean annual performance, with averaged F1 scores of 0.258±0.156, 0.253±0.153, and 0.236±0.143 for 2021, 2022, and 2023, respectively. This indicates that closer proximity to the reference datasets correlates with better overlap.

Table 4: Overview of validation results with validation subset, region, precision, recall, and f1- metrics, as well as number of true positive (TP), false positive (FP), and false negative (FN) features. BI: Banks Island, NW VI: Northwest Victoria Island, PR: Paulatuk region, BM: Bluenose Moraine, RM / PP: Richardson Mountains / Peel Plateau.

*Intersecting DARTS coverage and classified as active in 2016.

Val Set	Sub Region	Precision	Recall	F1	Features in the validation set [#]*
Val 1	-	0.548	-	-	2010
Val 2	#1	0.773±0.139	0.392±0.057	0.519±0.078	31
Val 2	#2	0.596±0.271	0.217±0.187	0.310±0.235	35
Val 2	#3	0.992±0.014	0.346±0.076	0.510±0.079	45
Val 2	#4	0.544±0.110	0.253±0.053	0.345±0.071	30
Val 2	#5	0	0	0	0
Val 2	#6	0.306±0.173	0.127±0.047	0.178±0.077	1
Val 2	#7	0	0	0	0
Val 2	#8	0	0	0	0
Val 3	BI	0.166±0.010	0.687±0.0223	0.267±0.01	3767
Val 3	NW VI	0.053±0.002	0.577±0.052	0.097±0.004	1174
Val 3	PR	0.287±0.029	0.439±0.027	0.346±0.023	123
Val 3	BM	0.351±0.001	0.578±0.059	0.436±0.017	215
Val 3	RM / PP	0.056±0.007	0.469±0.062	0.099±0.010	534

Table 5: Detailed analysis of false positives with manually assigned class type.

Category	Features [#]	Fraction of FP [%]
Bare Ground	975	64.44
Lake	119	7.87
River	107	7.07
Other	73	4.82

Periglacial Landform	62	4.1
Sea	48	3.17
Uncertain	43	2.84
Vegetation	30	1.98
SUM	**1513**	**100**

Discussion

Validation and dataset accuracy

Here we present the first version of a large-scale, automatically derived dataset of retrogressive thaw slumps (RTS) and active layer detachments (ALD) in circum-arctic hillslope thermokarst hotspots. This dataset is unique in its combination of multiannual coverage and extensive spatial extent.

Although the validation metrics show varying accuracies with F1 scores ranging from 0 to 0.519 on external validation sets, we still consider this product valuable in many regions. RTS and ALD are challenging targets for object detection and segmentation due to their sparsity and occurrence across diverse geographies. This is characterized by variations in vegetation, geology, substrates, soil moisture, and feature size and shape (Nesterova et al., 2024).

Validation against external datasets, including one external and two internal sources, proved challenging. Creating labeled or reference datasets for RTS is particularly difficult, requiring clear instructions, and even then, inconsistent labeling among different experts remains problematic and calls for standardized labeling protocols in the future (Nitze, Van Der Sluijs, et al., 2024). The difference in temporal overlap, e.g., in comparison to the Lewkowicz dataset, which furthermore consisted of point locations, may have further contributed to a mismatch of otherwise true positive overlapping features.

The variation in the ratio between precision and recall in the reference datasets, e.g., with higher precision than recall for internal Validation Set 2, which was based on VHR imagery, versus the other way around when compared to the external Validation Set 3 by (Lewkowicz, 2024a), which was based on lower spatial resolution data. In comparison, our training time validation was much more balanced and also exhibited better accuracies than the dataset validation. The training time validation metrics are similar to, albeit a bit lower than, similar studies, which are segmenting RTS (Huang et al., 2021; Witharana et al., 2022; Yang et al., 2023).

These validation issues highlight the need for specific benchmarks and consistent community efforts to improve and streamline permafrost-related detection and monitoring processes. Generally, in the remote sensing community, several landcover-oriented benchmark datasets have been released recently, such as the more generalistic BigEarthNet, the more regionally focused EuroSAT (Helber et al., 2019), and the polar research-focused ArcticNet (Jiang et al., 2019). Similarly, strategies or frameworks for benchmarking have also spawned, such as Major TOM (Francis & Czerkawski, 2024). However, specific permafrost landscape benchmark datasets do not yet exist, though some activities, such as pooling labels and creating quasi-benchmark and training datasets have been started (Yang et al., 2024). The intense dynamics of ALD and RTS, ambiguity of these erosion features, and the need for commercial satellite data in most cases make this a challenging task.

Research Potential

To the best of our knowledge, our dataset is the first to realistically quantify the number, area, and distribution of RTS and ALD in hotspots around the pan-arctic with sufficient spatial resolution for the target features. With multitemporal coverage from 2021 to 2023 across almost 900,000 km², it provides the opportunity for basic time-series analysis across a large spatial domain. Single coverage during this period expands even further to over 1.6 million km². Although the DARTS dataset covers only a fraction of the circum-arctic permafrost region, estimated to be between 14 million km² (Obu, 2021) and 23 million km² (Zhang et al., 2000), we expect to include a significant portion of RTS and ALD in our dataset due to their high clustering and concentration, as well as our thorough site selection. This large quantity will allow improved systematic analysis of the distribution of hillslope thermokarst and its key drivers and influencing factors, as demonstrated by (Makopoulou et al., 2024).

Given that the presence of RTS is closely tied to massive ground ice, our dataset can serve as a proxy for better understanding ground-ice distribution—one of the most significant unresolved puzzles in permafrost research (ref). As our dataset utilizes single satellite images as its primary input, representing only the spatial extent and dynamics, it cannot directly address volumetric changes since ALD and particularly RTS are three-dimensional features. Previous studies have explored the allometric scaling of 2D RTS information toward eroded volume estimates and found non-linear relationships (Van Der Sluijs et al., 2023).

Integrating our dataset with datasets and analyses explicitly measuring volumetric changes, e.g., (Bernhard et al., 2020, 2022; Dai et al., 2024; Huang et al., 2023), will create significant synergies by combining higher temporal and spatial resolution optical data with volumetric information derived from differential DEM data. The integration of volumetric changes is particularly important for the carbon cycle community, where quantification of RTS-related carbon fluxes is mostly limited to individual RTS or smaller clusters so far (Jensen et al., 2014; Ramage et al., 2018). Therefore, our dataset can help scale and extrapolate these local studies to much more meaningful sample sizes, as attempted in (Beer et al., 2023), but with more refined and pan-arctic data.

Dataset improvement and outlook

Our DARTS dataset in version v1 provides good quality RTS data but is not without misclassifications. While it worked well in RTS rich regions where RTS are typically bare ground surrounded by vegetation and along water bodies, it had more challenges with other regions. Challenges are particularly found in mountainous terrain where there is less contrast between a potentially RTS feature and its surroundings. Hence, current misclassifications typically showed up on rock outcrops and similar settings. The dataset therefore has to be used carefully in mountainous terrain with a lot of bare ground. In permafrost areas with more vegetation cover, e.g. tundra-covered Yedoma or ancient moraines, we are confident about the quality of detection algorithm and our dataset based on validation and visual inspection. Smaller water bodies like ponds, particularly with high sediment loads, were sometimes identified as another type of false positives due to large visual similarity with RTS.

Our labeling efforts for the current DARTS version primarily focused on positive labels, sampling RTS hotspots with numerous RTS and ALD examples. To address false positives, we have begun incorporating more RTS-free regions and will expand these further in the future. However, bare ground false detections remain prevalent. To further improve accuracy, we plan to include additional regions with few or no ALD and RTS, helping the model distinguish between genuine RTS patterns and similar-looking non-RTS features. Incorporating additional true ALD and RTS instances into the label dataset could further enhance model performance. Our dataset facilitates the identification of these features and accelerates the labeling process for positive RTS and ALD instances.

In our processing chain we were able to overcome the issue of abundant false positives with model ensembling, which has been successfully used in traditional machine-learning, e.g. in random forest models (Breiman, 2001). Although we simply averaged two model outputs, the impact of noise and model hallucinations were substantially minimized. Further automated cleaning of image edges and detections over water bodies, helped to clean the dataset to a much higher quality.

For future work, we propose exploring semi-supervised learning as an efficient way of working with a limited amount of labeled data that can serve as a start and gets expanded by iterative self-training in the model. This approach has been found to outperform supervised deep-learning models (Heidler et al., 2024) and could be particularly useful for our dataset. Semi-supervised learning might be especially beneficial in the permafrost domain, where labels are sparse for a very large spatial region with diverse landscapes.

The multi-temporal aspect of our dataset presents further potential for improvement. In its current iteration, the dataset is temporally agnostic, with deep-learning models considering only single observations despite some regions having multi-temporal labels. We have implicitly introduced temporal information through the Landsat trend layer, albeit at a lower spatial resolution and over a fixed 20-year period.

Incorporating real time-series information could prove highly beneficial, as we are dealing with dynamic landscape features whose temporal change patterns serve as strong indicators of their presence, particularly when compared to stable rock outcrops—the main source of errors. Strategies, which can help to address this may include utilizing multi-temporal information in the post-processing step, where detected output features are compared, overlapped, and subjected to specific rules requiring recurrence and slight changes. This approach has been applied by (Huang et al., 2021) for RTS detection on the Qinghai-Tibetan Plateau. Alternatively, it would be useful to implement temporal attention, a more explicit method incorporated in new deep learning architectures, such as those used in the Prithvi foundation model (Jakubik et al., 2023). Generally the use of vision transformers allows for integrating more variable information, such as location embeddings e.g. in Satclip (Klemmer et al., 2024), which might further boost performance and integrate real geography in addition to pure image analysis.

Data sources

For our dataset, we utilized multispectral PlanetScope imagery at 3-5 m spatial resolution, complemented by derived information from the ArcticDEM. This spatial resolution offers a good compromise between data volume and target size. Higher resolution data, such as that used by (Witharana et al., 2022), likely improves the detection of RTS and ALD, as erosion structures become easier to discern. However, such data presents significant challenges in terms of access (license restricted use), management, and processing, due to its size and restricted accessibility.

While PlanetScope data has a very useful spatial and temporal resolution for our study targets, this data is inaccessible to most researchers due to its commercial nature. We obtained data access through own data purchases, researcher access programs, the NASA CSDA program, and University of Illinois to cover a sizeable but still not exhaustive multitemporal area in the Arctic, however, working with such a large amount of data and a complex way of sourcing it for research purposes is not feasible for many users. Publicly available data sources, such as from ESA's Sentinel-2 with a somewhat lower 10m spatial resolution, might serve as an highly useful alternative. Data access is free and much easier, and freely available preprocessing resources and tools such as Google Earthengine are available. Additionally, the provision of free cloud access simplifies workflows significantly, as it reduces the need to locally store and manage large datasets. Also, thoroughly preprocessed mosaics (COPERNICUS) and spectrally harmonized data are available. However, the lower spatial resolution could be critical for smaller features, potentially leading to less accurate detection.

In the AI/DL realm, super-resolution techniques have been explored to enhance the spatial resolution of satellite data (Kyzivat & Smith, 2023; Mullen et al., 2023). Given the relatively small gap between Sentinel-2 and PlanetScope resolutions, this approach might be feasible to overcome resolution limitations. In the Arctic permafrost domain, super-resolution has been successfully applied to bridge the scales from 30m Landsat to 3m PlanetScope resolution for long-term surface water change research (Kyzivat & Smith, 2023). This technique could potentially be adapted to improve the detection of smaller RTS and ALD features using publicly available data sources.

Conclusion

The detection and quantification of RTS and ALD across the pan-arctic permafrost region is a hot research topic because they are robust indicators of permafrost and now becoming possible to detect with the described AI based methods. Our publicly available dataset represents the first step toward a realistic quantification and understanding of these erosion features in this vast region. The dataset is accessible through the Arctic Data Center's Permafrost Discovery Gateway, available to visualize in full or to download in standard formats (Geopackage and Parquet) for maximum reusability, and includes exhaustive metadata. Currently, it covers a maximum area of 1.6 million km² with multitemporal coverage of approximately 900,000 km², encompassing a substantial portion of where RTS occur in the circum-arctic.

This dataset will facilitate research on various topics in permafrost studies, including carbon dynamics, local geohazards, and enhancing our understanding of ground-ice distribution, one of the most significant unresolved questions in this field. Although validation metrics show relatively low F1-scores for object detection, ranging from 0 to 0.519, we remain confident in the quality of our dataset due to its scale and the absence of dedicated reference or benchmark datasets.

The dataset is a *living* dataset, which will receive frequent updates. We are actively working on expanding its spatial and temporal dimensions by integrating Sentinel-2 data and improving the underlying deep-learning models through testing state-of-the-art transformers and semi-supervised learning approaches. In future versions, we envision integrating volumetric changes to better represent the true volumetric nature of RTS.

With further additions of more spatially distributed training labels, we anticipate significant improvements, particularly in regions with sparse RTS/ALD presence and where rock outcrops are evident. By making the code and deep learning models available, we aim to adhere to the open-data and open-source movement. Due to license restrictions on the PlanetScope data, we cannot share the raw data; however, the processing workflow can be reused and adapted to enhance research efforts.

Version 1 of our dataset represents a leap toward comprehensive circum-arctic RTS and ALD monitoring. As technical advancements continue, more datasets are under development that will help address pressing questions and fill existing knowledge gaps in the rapidly evolving circum-arctic permafrost region.

Dataset + Code + Model checkpoints

Dataset

The DARTS dataset in version 1 is publicly available on the Arctic Data Center (arcticdata.io) available through the following DOI Link: https://doi.org/10.18739/A2RR1PP44

For exploring/visualizing and downloading portions of the dataset, please visit the Permafrost Discovery Gateway (in preparation)

Training Labels

Github: https://github.com/initze/ML_training_labels

Zenodo: https://doi.org/10.5281/zenodo.12706221

Processing Code

Github: https://github.com/initze/thaw-slump-segmentation

Zenodo: Nitze, I., Heidler, K., Küpper, J., & Hölzer, T. (2024). *DARTS RTS AI segmentation code* (Version v0.11.0) [Computer software]. Zenodo. https://doi.org/10.5281/ZENODO.13935921

Model checkpoints

https://drive.google.com/file/d/1yprV_At6mFvZSHvvVBURlQ0Lrl0SCKo1/view?usp=sharing (330MB)

Acknowledgements

IN, KH and GG: HGF AI-CORE, BMWK ML4EARTH

IN, GG, AL: NSF Navigating the New Arctic awards #1927872 #2052107

IN, JK, TH, GG, AL: google.org Impact Challenge on Climate Innovation to the Permafrost Discovery Gateway development team

NN: DAAD stipend

ML: NSF#1928048, NASA #80NSSC22K1254

PlanetScope data were bought through HGF AI-CORE, provided through the NASA CSDA program, provided by U Illinois, and provided through Planet Research Program.

MACS aerial image data used for validation was acquired through AWI Perma-X campaigns with Polar-6 in Alaska and NW Canada in 2021, 2023, and 2024.

We acknowledge support by Potsdam InnoLab for Arctic Research infrastructure funds provided through the Ministry for Science, Research, and Culture of Brandenburg.

We used perplexity.ai for text and language editing

References

Babkina, E. A., Leibman, M. O., Dvornikov, Yu. A., Fakashchuk, N. Yu., Khairullin, R. R., & Khomutov, A. V. (2019). Activation of Cryogenic Processes in Central Yamal as a Result of Regional and Local Change in Climate and Thermal State of Permafrost. *Russian Meteorology and Hydrology*, *44*(4), 283–290. https://doi.org/10.3103/S1068373919040083

Barth, B., Sophia, Nitze, I., Juhls, B., Runge, A., & Grosse, G. (in review). *Rapid changes in retrogressive thaw slump dynamics in the Russian High Arctic based on very high-resolution remote sensing*.

Beer, C., Runge, A., Grosse, G., Hugelius, G., & Knoblauch, C. (2023). Carbon dioxide release from retrogressive thaw slumps in Siberia. *Environmental Research Letters*, *18*(10), 104053.

https://doi.org/10.1088/1748-9326/acfdbb

Bernhard, P., Zwieback, S., Bergner, N., & Hajnsek, I. (2022). Assessing volumetric change distributions and scaling relations of retrogressive thaw slumps across the Arctic. *The Cryosphere*, *16*(1), 1–15. https://doi.org/10.5194/tc-16-1-2022

Bernhard, P., Zwieback, S., Leinss, S., & Hajnsek, I. (2020). Mapping Retrogressive Thaw Slumps Using Single-Pass TanDEM-X Observations. *IEEE Journal of Selected Topics in Applied Earth Observations and Remote Sensing*, *13*, 3263–3280. https://doi.org/10.1109/JSTARS.2020.3000648

Biskaborn, B. K., Smith, S. L., Noetzli, J., Matthes, H., Vieira, G., Streletskiy, D. A., Schoeneich, P., Romanovsky, V. E., Lewkowicz, A. G., Abramov, A., Allard, M., Boike, J., Cable, W. L., Christiansen, H. H., Delaloye, R., Diekmann, B., Drozdov, D., Etzelmüller, B., Grosse, G., … Lantuit, H. (2019). Permafrost is warming at a global scale. *Nature Communications*, *10*(1), 264. https://doi.org/10.1038/s41467-018-08240-4

Breiman, L. (2001). Random Forests. *Machine Learning*, *45*(1), 5–32. https://doi.org/10.1023/A:1010933404324

Burn, C. R., & Lewkowicz, A. G. (1990). CANADIAN LANDFORM EXAMPLES - 17 RETROGRESSIVE THAW SLUMPS. *The Canadian Geographer/Le Géographe Canadien*, *34*(3), 273–276. https://doi.org/10.1111/j.1541-0064.1990.tb01092.x

Buslaev, A., Iglovikov, V. I., Khvedchenya, E., Parinov, A., Druzhinin, M., & Kalinin, A. A. (2020). Albumentations: Fast and Flexible Image Augmentations. *Information*, *11*(2), Article 2. https://doi.org/10.3390/info11020125

Cong, Y., Khanna, S., Meng, C., Liu, P., Rozi, E., He, Y., Burke, M., Lobell, D. B., & Ermon, S. (2022). *SatMAE: Pre-training Transformers for Temporal and Multi-Spectral Satellite Imagery* (Version 3). arXiv. https://doi.org/10.48550/ARXIV.2207.08051

Dai, C., Howat, I. M., Van Der Sluijs, J., Liljedahl, A. K., Higman, B., Freymueller, J. T., Ward Jones, M. K., Kokelj, S. V., Boike, J., Walker, B., & Marsh, P. (2024). Applications of ArcticDEM for measuring volcanic dynamics, landslides, retrogressive thaw slumps, snowdrifts, and vegetation heights. *Science of Remote Sensing*, *9*, 100130. https://doi.org/10.1016/j.srs.2024.100130

Detlefsen, N., Borovec, J., Schock, J., Jha, A., Koker, T., Di Liello, L., Stancl, D., Quan, C., Grechkin, M., & Falcon, W. (2022). TorchMetrics—Measuring Reproducibility in PyTorch. *Journal of Open Source Software*, *7*(70), 4101. https://doi.org/10.21105/joss.04101

Francis, A., & Czerkawski, M. (2024). *Major TOM: Expandable Datasets for Earth Observation* (No. arXiv:2402.12095). arXiv. http://arxiv.org/abs/2402.12095

Heidler, K., Nitze, I., Grosse, G., & Zhu, X. X. (2024). PixelDINO: Semi-Supervised Semantic Segmentation for Detecting Permafrost Disturbances in the Arctic. *IEEE Transactions on Geoscience and Remote Sensing*, 1–1. https://doi.org/10.1109/TGRS.2024.3448294

Helber, P., Bischke, B., Dengel, A., & Borth, D. (2019). EuroSAT: A Novel Dataset and Deep Learning Benchmark for Land Use and Land Cover Classification. *IEEE Journal of Selected Topics in Applied Earth Observations and Remote Sensing*, *12*(7), 2217–2226. IEEE Journal of Selected Topics in Applied Earth Observations and Remote Sensing. https://doi.org/10.1109/JSTARS.2019.2918242

Huang, L., Liu, L., Luo, J., Lin, Z., & Niu, F. (2021). Automatically quantifying evolution of retrogressive thaw slumps in Beiluhe (Tibetan Plateau) from multi-temporal CubeSat images. *International Journal of Applied Earth Observation and Geoinformation*, *102*, 102399. https://doi.org/10.1016/j.jag.2021.102399

Huang, L., Luo, J., Lin, Z., Niu, F., & Liu, L. (2020). Using deep learning to map retrogressive thaw slumps in the Beiluhe region (Tibetan Plateau) from CubeSat images. *Remote Sensing of Environment*, *237*, 111534. https://doi.org/10.1016/j.rse.2019.111534

Huang, L., Willis, M. J., Li, G., Lantz, T. C., Schaefer, K., Wig, E., Cao, G., & Tiampo, K. F. (2023). Identifying active retrogressive thaw slumps from ArcticDEM. *ISPRS Journal of Photogrammetry and Remote Sensing*, *205*, 301–316. https://doi.org/10.1016/j.isprsjprs.2023.10.008

Huete, A., Didan, K., Miura, T., Rodriguez, E. P., Gao, X., & Ferreira, L. G. (2002). Overview of the radiometric and biophysical performance of the MODIS vegetation indices. *Remote Sensing of Environment*, *83*(1–2), 195–213. https://doi.org/10.1016/S0034-4257(02)00096-2

Iakubovskii, P. (2019). Segmentation Models. In *GitHub repository*. GitHub. https://github.com/qubvel/segmentation_models

Jakubik, J., Roy, S., Phillips, C. E., Fraccaro, P., Godwin, D., Zadrozny, B., Szwarcman, D., Gomes, C., Nyirjesy, G., Edwards, B., Kimura, D., Simumba, N., Chu, L., Mukkavilli, S. K., Lambhate, D., Das, K., Bangalore, R., Oliveira, D., Muszynski, M., … Ramachandran, R. (2023). *Foundation Models for Generalist Geospatial Artificial Intelligence* (No. arXiv:2310.18660). arXiv. http://arxiv.org/abs/2310.18660

Jensen, A. E., Lohse, K. A., Crosby, B. T., & Mora, C. I. (2014). Variations in soil carbon dioxide efflux across a thaw slump chronosequence in northwestern Alaska. *Environmental Research Letters*, *9*(2), 025001. https://doi.org/10.1088/1748-9326/9/2/025001

Jiang, Z., Von Ness, K., Loisel, J., & Wang, Z. (2019). ArcticNet: A Deep Learning Solution to Classify the Arctic Area. *Proceedings of the IEEE/CVF Conference on Computer Vision and Pattern Recognition Workshops*, 38–47. https://openaccess.thecvf.com/content_CVPRW_2019/html/DOAI/Jiang_ArcticNet_A_Deep_Learning_Solution_to_Classify_the_Arctic_Area_CVPRW_2019_paper.html

Karra, K., Kontgis, C., Statman-Weil, Z., Mazzariello, J. C., Mathis, M., & Brumby, S. P. (2021). Global land use / land cover with Sentinel 2 and deep learning. *2021 IEEE International Geoscience and Remote Sensing Symposium IGARSS*, 4704–4707. https://doi.org/10.1109/IGARSS47720.2021.9553499

Kerfoot, D. E. (1969). *The geomorphology and permafrost conditions of Garry Island, N.W.T.* https://doi.org/10.14288/1.0102152

Kizyakov, A. I., Korotaev, M. V., Wetterich, S., Opel, T., Pravikova, N. V., Fritz, M., Lupachev, A. V., Günther, F., Shepelev, A. G., Syromyatnikov, I. I., Fedorov, A. N., Zimin, M. V., & Grosse, G. (2024). Characterizing Batagay megaslump topography dynamics and matter fluxes at high spatial resolution using a multidisciplinary approach of permafrost field observations, remote sensing and 3D geological modeling. *Geomorphology*, 109183. https://doi.org/10.1016/j.geomorph.2024.109183

Klemmer, K., Rolf, E., Robinson, C., Mackey, L., & Rußwurm, M. (2024). *SatCLIP: Global, General-Purpose Location Embeddings with Satellite Imagery* (No. arXiv:2311.17179). arXiv. http://arxiv.org/abs/2311.17179

Kokelj, S. V., Gingras-Hill, T., Daly, S. V., Morse, P., Wolfe, S., Rudy, A. C. A., Van Der Sluijs, J., Weiss, N., O'Neill, B., Baltzer, J., Lantz, T. C., Gibson, C., Cazon, D., Fraser, R. H., Froese, D. G., Giff, G., Klengenberg, C., Lamoureux, S. F., Quinton, W., … Young, J. (2023). The Northwest Territories Thermokarst Mapping Collective: A northern-driven mapping collaborative toward understanding the effects of permafrost thaw. *Arctic Science*, AS-2023-0009. https://doi.org/10.1139/AS-2023-0009

Kokelj, S. V., & Jorgenson, M. T. (2013). Advances in Thermokarst Research. *Permafrost and Periglacial Processes*, *24*(2), 108–119. https://doi.org/10.1002/ppp.1779

Kokelj, S. V., Kokoszka, J., van der Sluijs, J., Rudy, A. C. A., Tunnicliffe, J., Shakil, S., Tank, S. E., & Zolkos, S. (2021). Thaw-driven mass wasting couples slopes with downstream systems, and effects propagate through Arctic drainage networks. *The Cryosphere*, *15*(7), 3059–3081. https://doi.org/10.5194/tc-15-3059-2021

Kokelj, S. V., Lantz, T. C., Tunnicliffe, J., Segal, R., & Lacelle, D. (2017). Climate-driven thaw of permafrost preserved glacial landscapes, northwestern Canada. *Geology*, *45*(4), 371–374. https://doi.org/10.1130/G38626.1

Kokelj, S. V., Tunnicliffe, J., Lacelle, D., Lantz, T. C., Chin, K. S., & Fraser, R. (2015). Increased precipitation drives mega slump development and destabilization of ice-rich permafrost terrain, northwestern Canada. *Global and Planetary Change*, *129*, 56–68. https://doi.org/10.1016/j.gloplacha.2015.02.008

Kyzivat, E. D., & Smith, Laurence. C. (2023). Contemporary and historical detection of small lakes using super resolution Landsat imagery: Promise and peril. *GIScience & Remote Sensing*, *60*(1), 2207288. https://doi.org/10.1080/15481603.2023.2207288

Lacelle, D., Bjornson, J., & Lauriol, B. (2010). Climatic and geomorphic factors affecting contemporary (1950-2004) activity of retrogressive thaw slumps on the Aklavik Plateau, Richardson Mountains, NWT, Canada: Climatic and Geomorphic Factors affecting Thaw Slump Activity. *Permafrost and Periglacial Processes*, *21*(1), 1–15. https://doi.org/10.1002/ppp.666

Lantuit, H., & Pollard, W. H. (2008). Fifty years of coastal erosion and retrogressive thaw slump activity on Herschel Island, southern Beaufort Sea, Yukon Territory, Canada. *Geomorphology*, *95*(1–2),

84–102. https://doi.org/10.1016/j.geomorph.2006.07.040

Lantz, T. C., & Kokelj, S. V. (2008). Increasing rates of retrogressive thaw slump activity in the Mackenzie Delta region, N.W.T., Canada. *Geophysical Research Letters*, *35*(6), L06502. https://doi.org/10.1029/2007GL032433

Leibman, M., Khomutov, A., & Kizyakov, A. (2014). Cryogenic Landslides in the West-Siberian Plain of Russia: Classification, Mechanisms, and Landforms. In W. Shan, Y. Guo, F. Wang, H. Marui, & A. Strom (Eds.), *Landslides in Cold Regions in the Context of Climate Change* (pp. 143–162). Springer International Publishing. https://doi.org/10.1007/978-3-319-00867-7_11

Lewkowicz, A. G. (2007). Dynamics of active‐layer detachment failures, Fosheim Peninsula, Ellesmere Island, Nunavut, Canada. *Permafrost and Periglacial Processes*, *18*(1), 89–103. https://doi.org/10.1002/ppp.578

Lewkowicz, A. G. (2024a). *Retrogressive thaw slump activity and related lake colour change in five areas of the western Canadian Arctic, v. 1.0 (1984-2018)* [Dataset]. Nordicana D. https://doi.org/10.5885/45888XD-C644C19F4F414D58

Lewkowicz, A. G. (2024b). *Retrogressive thaw slump activity in the western Canadian Arctic (1984-2016)*. https://doi.org/10.31223/X5H11S

Lewkowicz, A. G., & Harris, C. (2005). Morphology and geotechnique of active-layer detachment failures in discontinuous and continuous permafrost, northern Canada. *Geomorphology*, *69*(1–4), 275–297. https://doi.org/10.1016/j.geomorph.2005.01.011

Lewkowicz, A. G., & Way, R. G. (2019). Extremes of summer climate trigger thousands of thermokarst landslides in a High Arctic environment. *Nature Communications*, *10*(1), Article 1. https://doi.org/10.1038/s41467-019-09314-7

Liu, Y., Qiu, H., Kamp, U., Wang, N., Wang, J., Huang, C., & Tang, B. (2024). Higher temperature sensitivity of retrogressive thaw slump activity in the Arctic compared to the Third Pole. *Science of The Total Environment*, *914*, 170007. https://doi.org/10.1016/j.scitotenv.2024.170007

Mackay, J. R. (1966). Segregated epigenetic ice and slumps in permafrost, Mackenzie Delta area, NWT. *Geographical Bulletin*, *8*, 59–80.

Makopoulou, E., Karjalainen, O., Elia, L., Blais‐Stevens, A., Lantz, T., Lipovsky, P., Lombardo, L., Nicu, I.

C., Rubensdotter, L., Rudy, A. C. A., & Hjort, J. (2024). Retrogressive thaw slump susceptibility in the northern hemisphere permafrost region. *Earth Surface Processes and Landforms*, esp.5890. https://doi.org/10.1002/esp.5890

Mullen, A. L., Watts, J. D., Rogers, B. M., Carroll, M. L., Elder, C. D., Noomah, J., Williams, Z., Caraballo-Vega, J. A., Bredder, A., Rickenbaugh, E., Levenson, E., Cooley, S. W., Hung, J. K. Y., Fiske, G., Potter, S., Yang, Y., Miller, C. E., Natali, S. M., Douglas, T. A., & Kyzivat, E. D. (2023). Using High-Resolution Satellite Imagery and Deep Learning to Track Dynamic Seasonality in Small Water Bodies. *Geophysical Research Letters*, *50*(7), e2022GL102327. https://doi.org/10.1029/2022GL102327

Nesterova, N., Khomutov, A., Leibman, M., Safonov, T., & Belova, N. (2021). THE INVENTORY OF RETROGRESSIVE THAW SLUMPS (THERMOCIRQUES) IN THE NORTH OF WEST SIBERIA BASED ON 2016-2018 SATELLITE IMAGERY MOSAIC. *Earth's Cryosphere*, *6*.

Nesterova, N., Leibman, M., Kizyakov, A., Lantuit, H., Tarasevich, I., Nitze, I., Veremeeva, A., & Grosse, G. (2024). *Review article: Retrogressive thaw slump theory and terminology* [Preprint]. Frozen ground/Geomorphology. https://doi.org/10.5194/egusphere-2023-2914

Nitze, I. (2024). *initze/ML_training_labels: V1.0* (Version v1.0) [Computer software]. Zenodo. https://doi.org/10.5281/ZENODO.12706221

Nitze, I., & Grosse, G. (2016). Detection of landscape dynamics in the Arctic Lena Delta with temporally dense Landsat time-series stacks. *Remote Sensing of Environment*, *181*, 27–41. https://doi.org/10.1016/j.rse.2016.03.038

Nitze, I., Grosse, G., Jones, B., Arp, C., Ulrich, M., Fedorov, A., & Veremeeva, A. (2017). Landsat-Based Trend Analysis of Lake Dynamics across Northern Permafrost Regions. *Remote Sensing*, *9*(7), 640. https://doi.org/10.3390/rs9070640

Nitze, I., Grosse, G., Jones, B. M., Romanovsky, V. E., & Boike, J. (2018). Remote sensing quantifies widespread abundance of permafrost region disturbances across the Arctic and Subarctic. *Nature Communications*, *9*(1), 5423. https://doi.org/10.1038/s41467-018-07663-3

Nitze, I., Heidler, K., Barth, S., & Grosse, G. (2021). Developing and Testing a Deep Learning Approach for Mapping Retrogressive Thaw Slumps. *Remote Sensing*, *13*(21).

https://doi.org/10.3390/rs13214294

Nitze, I., Heidler, K., Küpper, J., & Hölzer, T. (2024). *DARTS RTS AI segmentation code* (Version v0.11.0) [Computer software]. Zenodo. https://doi.org/10.5281/ZENODO.13935921

Nitze, I., Lübker, T., & Grosse, G. (2024). *Pan-Arctic Visualization of Landscape Change (2003-2022), Arctic PASSION Permafrost Service* (p. 16 data points) [Text/tab-separated-values]. [object Object]. https://doi.org/10.1594/PANGAEA.964814

Nitze, I., Van Der Sluijs, J., Barth, S., Bernhard, P., Huang, L., Lara, M., Kizyakov, A., Runge, A., Veremeeva, A., Ward Jones, M., Witharana, C., Xia, Z., & Liljedahl, A. (2024). *A labeling intercomparison of retrogressive thaw slumps by a diverse group of domain experts*. https://doi.org/10.31223/X55M4P

Obu, J. (2021). How Much of the Earth's Surface is Underlain by Permafrost? *Journal of Geophysical Research: Earth Surface*, *126*(5). https://doi.org/10.1029/2021JF006123

Obu, J., Westermann, S., Kääb, A., & Bartsch, A. (2018). *Ground Temperature Map, 2000-2016, Northern Hemisphere Permafrost* (p. 40 data points) [Text/tab-separated-values]. PANGAEA - Data Publisher for Earth & Environmental Science. https://doi.org/10.1594/PANGAEA.888600

Paszke, A., Gross, S., Massa, F., Lerer, A., Bradbury, J., Chanan, G., Killeen, T., Lin, Z., Gimelshein, N., Antiga, L., Desmaison, A., Köpf, A., Yang, E., DeVito, Z., Raison, M., Tejani, A., Chilamkurthy, S., Steiner, B., Fang, L., … Chintala, S. (2019). PyTorch: An Imperative Style, High-Performance Deep Learning Library. *arXiv:1912.01703 [Cs, Stat]*. http://arxiv.org/abs/1912.01703

Planet Team. (2017). *Planet Application Program Interface: In Space for Life on Earth*. Planet. https://api.planet.com

Porter, C., Morin, P., Howat, I., Noh, M.-J., Bates, B., Peterman, K., Keesey, S., Schlenk, M., Gardiner, J., Tomko, K., Willis, M., Kelleher, C., Cloutier, M., Husby, E., Foga, S., Nakamura, H., Platson, M., Wethington, M., Williamson, C., … Bojesen, M. (2018). *ArcticDEM* [Dataset]. Harvard Dataverse. https://doi.org/10.7910/DVN/OHHUKH

Ramage, J. L., Irrgang, A. M., Morgenstern, A., & Lantuit, H. (2018). Increasing coastal slump activity impacts the release of sediment and organic carbon into the Arctic Ocean. *Biogeosciences*, *15*(5), 1483–1495. https://doi.org/10.5194/bg-15-1483-2018

Roy, S., Gandhi, U., Swetnam, T., Somasundaram, D., & Saah, A. (2024). *samapriya/awesome-gee-community-datasets: Community Catalog* (Version 2.8.0) [Computer software]. Zenodo. https://doi.org/10.5281/ZENODO.13218907

Runge, A., Nitze, I., & Grosse, G. (2022). Remote sensing annual dynamics of rapid permafrost thaw disturbances with LandTrendr. *Remote Sensing of Environment*, *268*, 112752. https://doi.org/10.1016/j.rse.2021.112752

Smith, S. L., O'Neill, H. B., Isaksen, K., Noetzli, J., & Romanovsky, V. E. (2022). The changing thermal state of permafrost. *Nature Reviews Earth & Environment*, *3*(1), 10–23. https://doi.org/10.1038/s43017-021-00240-1

Swanson, D. K. (2021). Permafrost thaw‐related slope failures in Alaska's Arctic National Parks. 1980–2019. *Permafrost and Periglacial Processes*, *32*(3), 392–406. https://doi.org/10.1002/ppp.2098

Swanson, D. K., & Nolan, M. (2018). Growth of Retrogressive Thaw Slumps in the Noatak Valley, Alaska, 2010–2016, Measured by Airborne Photogrammetry. *Remote Sensing*, *10*(7), 983. https://doi.org/10.3390/rs10070983

Turetsky, M. R., Abbott, B. W., Jones, M. C., Walter Anthony, K., Olefeldt, D., Schuur, E. A. G., Koven, C., McGuire, A. D., Grosse, G., Kuhry, P., Hugelius, G., Lawrence, D. M., Gibson, C., & Sannel, A. B. K. (2019). Permafrost collapse is accelerating carbon release. *Nature*, *569*(7754), 32–34. https://doi.org/10.1038/d41586-019-01313-4

Van Der Sluijs, J., Kokelj, S. V., & Tunnicliffe, J. F. (2023). Allometric scaling of retrogressive thaw slumps. *The Cryosphere*, *17*(11), 4511–4533. https://doi.org/10.5194/tc-17-4511-2023

Ward Jones, M. K., Pollard, W. H., & Jones, B. M. (2019). Rapid initialization of retrogressive thaw slumps in the Canadian high Arctic and their response to climate and terrain factors. *Environmental Research Letters*, *14*(5), 055006. https://doi.org/10.1088/1748-9326/ab12fd

Witharana, C., Udawalpola, M. R., Liljedahl, A. K., Jones, M. K. W., Jones, B. M., Hasan, A., Joshi, D., & Manos, E. (2022). Automated Detection of Retrogressive Thaw Slumps in the High Arctic Using High-Resolution Satellite Imagery. *Remote Sensing*, *14*(17), 4132. https://doi.org/10.3390/rs14174132

Xia, Z., Liu, L., Mu, C., Peng, X., Zhao, Z., Huang, L., Luo, J., & Fan, C. (2024). Widespread and Rapid Activities of Retrogressive Thaw Slumps on the Qinghai‐Tibet Plateau From 2016 to 2022. *Geophysical Research Letters*, *51*(17), e2024GL109616. https://doi.org/10.1029/2024GL109616

Yang, Y., Rodenhizer, H., & Dean, J. (2024). *Arctic Retrogressive Thaw Slumps (ARTS): Digitisations of pan-Arctic retrogressive thaw slumps, 1985-2021* [Text/xml]. NSF Arctic Data Center. https://doi.org/10.18739/A2PK0738B

Yang, Y., Rogers, B. M., Fiske, G., Watts, J., Potter, S., Windholz, T., Mullen, A., Nitze, I., & Natali, S. M. (2023). Mapping retrogressive thaw slumps using deep neural networks. *Remote Sensing of Environment*, *288*, 113495. https://doi.org/10.1016/j.rse.2023.113495

Zhang, T., Heginbottom, J. A., Barry, R. G., & Brown, J. (2000). Further statistics on the distribution of permafrost and ground ice in the Northern Hemisphere [1]. *Polar Geography*, *24*(2), 126–131. https://doi.org/10.1080/10889370009377692

Zhou, Z., Rahman Siddiquee, M. M., Tajbakhsh, N., & Liang, J. (2018). UNet++: A Nested U-Net Architecture for Medical Image Segmentation. In D. Stoyanov, Z. Taylor, G. Carneiro, T. Syeda-Mahmood, A. Martel, L. Maier-Hein, J. M. R. S. Tavares, A. Bradley, J. P. Papa, V. Belagiannis, J. C. Nascimento, Z. Lu, S. Conjeti, M. Moradi, H. Greenspan, & A. Madabhushi (Eds.), *Deep Learning in Medical Image Analysis and Multimodal Learning for Clinical Decision Support* (Vol. 11045, pp. 3–11). Springer International Publishing. https://doi.org/10.1007/978-3-030-00889-5_1

Supplementary Material

Supplementary Table S1: Overview of training datasets with iteration, number of unique image scenes, number of features (RTS/ALD), number of images with and without labels, and the date range.

	Unique images [#]	Features [#]	Images with labels [#]	Images without labels [#]	Date range
iteration001	169	2182	149	20	2018-07-02 to 2019-09-28

iteration002	6	743	6	0	2020-07-22 to 2021-07-15
iteration003	4	410	4	0	2020-08-14 to 2021-08-06
iteration004	2	204	2	0	2021-07-21 to 2021-08-06
iteration005	5	141	0	5	2021-07-12 to 2022-07-25
iteration006	12	69	3	9	2022-07-25 to 2022-08-13

Dataset description

Supplementary Table S2: Detailed overview of DARTS Level1 dataset attributes, with attribute name, data type, description, and example..

Column Name	Data Type	Description	Example
id	Integer	A unique identifier for each feature in the dataset.	0
id_geohash	String	A geospatial hash code representing the location of the feature.	fqx77bgsy65k
date	String	The date associated with the feature, in YYYY-MM-DD format.	2023-08-15
year	Integer	The year extracted from the date column.	2023
area_m2	Float	The area of the feature in square meters.	1116.89
area_ha	Float	The area of the feature in hectares.	0.1117
DARTS_dataset_version	String	The version of the DARTS dataset used.	v1.0
DARTS_AI_model_version	String	The version of the RTS AI model used for processing the data.	RTS_v6_ensemble_v3_filterWater

DARTS_AI_model_threshold	String	The threshold value used by the RTS AI model.	0.5
feature_information	String	Additional information related to the DARTS dataset and processing.	RTS/ALD footprint - individual image - Level 1
image_source	String	The source of the image associated with the feature.	PlanetScope
image_id	String	The identifier of the input image image associated with this feature.	20230815_191951_90_24af
geometry	Geometry	The geometry column containing spatial data representing the feature's location.	POLYGON ((-68.38536206601792 82.13895427289602...

Supplementary Table S3: Detailed overview of DARTS Level1 dataset attributes, with attribute name, data type, description, and example.

Column Name	Data Type	Description	Example
id	Integer	A unique identifier for each feature in the dataset.	35676
id_geohash	String	A geospatial hash code representing the location of the feature.	ck8qq7v98kyz
year	Integer	The year associated with the feature, indicating when the observations were made.	2022
area_m2	Float	The area of the feature in square meters.	49805.441
area_ha	Float	The area of the feature in hectares.	4.980
num_observations	Integer	The total number of observations recorded for the feature, useful for statistical analysis.	3
earliest_date	String	The earliest date of observation associated with the feature, in a string format.	2022-07-19

latest_date	String	The latest date of observation associated with the feature, in a string format.	2022-08-23
DARTS_dataset_version	String	The version of the DARTS dataset.	v1.0
DARTS_AI_model_version	String	The version of the RTS AI model used for processing the data.	RTS_v6_ensemble_v3_filterWater
DARTS_AI_model_threshold	String	The threshold value used by the RTS AI model.	0.5
feature_information	String	Additional information related to the RTS dataset and processing.	RTS/ALD footprint - annually aggregated - Level 2
image_source	String	The source of the image associated with the feature.	PlanetScope
geometry	Geometry	The geometry column containing spatial data representing the feature's location.	POLYGON ((-172.459812820259564.70119955501342...

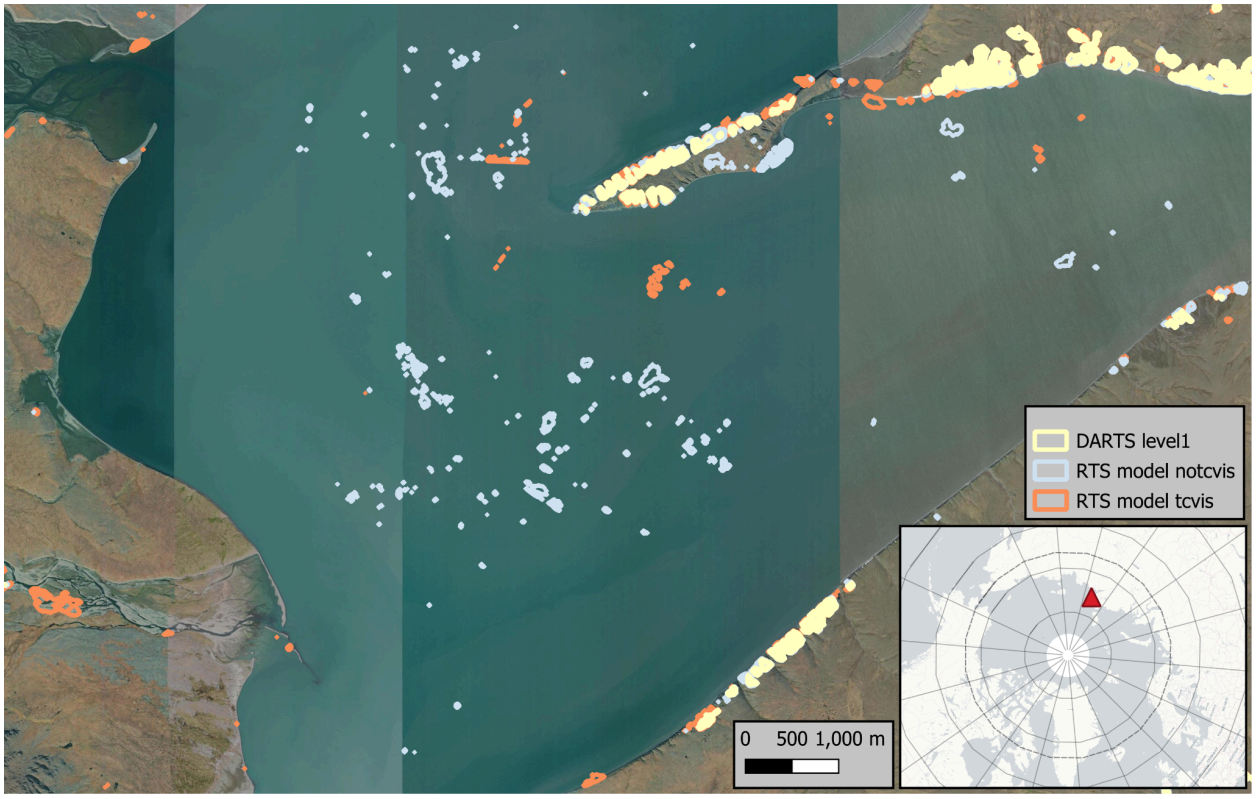

Supplementary Figure S1: Comparison of raw deep learning model output of *tcvis* (orange) and *notcvis* (light blue) models before cleaning and ensembling versus final DARTS Level 1 dataset, which was ensembled by the raw tcvis and notcvis model inputs and underwent several cleaning steps. This example is taken from the eastern Taymyr peninsula (75.65 °N, 112.97 °E). Background Map: *ESRI Satellite*.

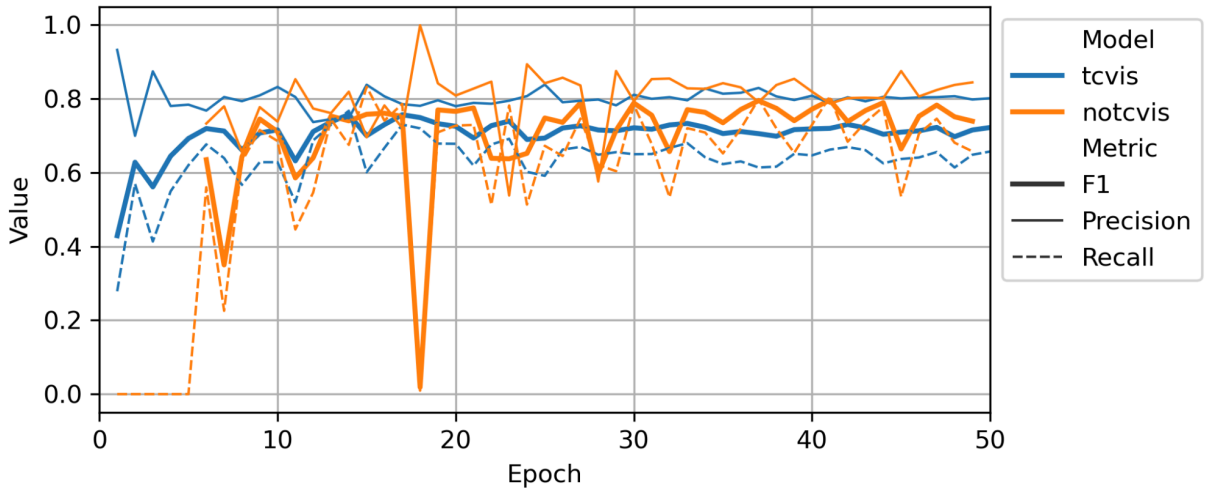

Supplementary Figure S2: Internal validation metrics of raw tcvis and notcvis deep-learning models.

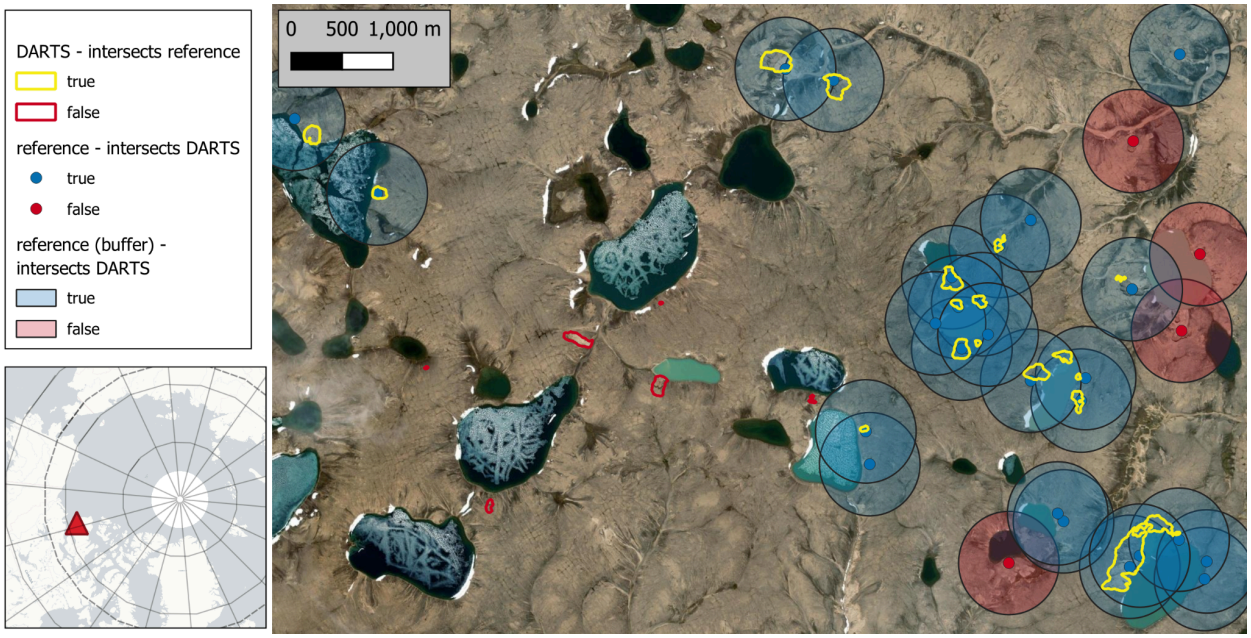

Supplementary Figure S3: Validation of DARTS dataset with the Lewkowicz et al, 2024 reference dataset on Banks Island (71.68 °N, 122.02 °W). DARTS true positives in yellow and reference true positives in blue (point location + 500m buffer) with mutual intersection. DARTS and reference false positives, where datasets do not intersect, are indicated in red. Background Map: *ESRI Satellite*.

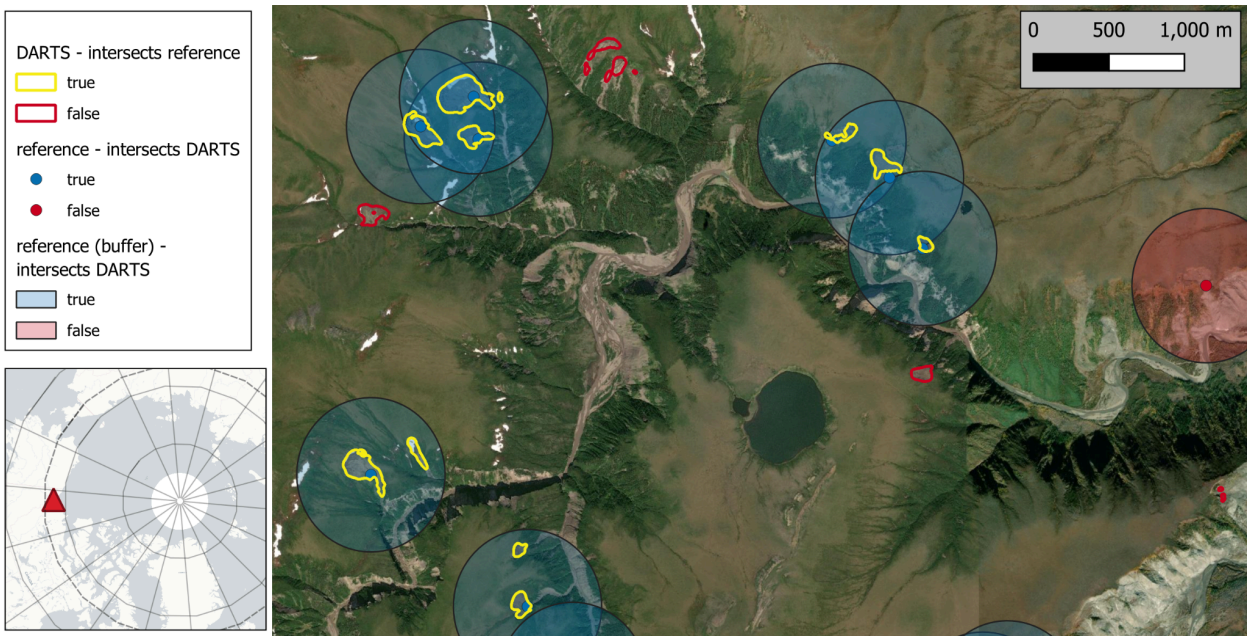

Supplementary Figure S4: Validation of DARTS dataset with the Lewkowicz et al, 2024 reference dataset on the Peel Plateau (68.21 °N, 135.62 °W). DARTS true positives in yellow and reference true positives in blue (point location + 500m buffer) with mutual intersection. DARTS and reference false positives, where datasets do not intersect, are indicated in red. Background Map: *ESRI Satellite*.

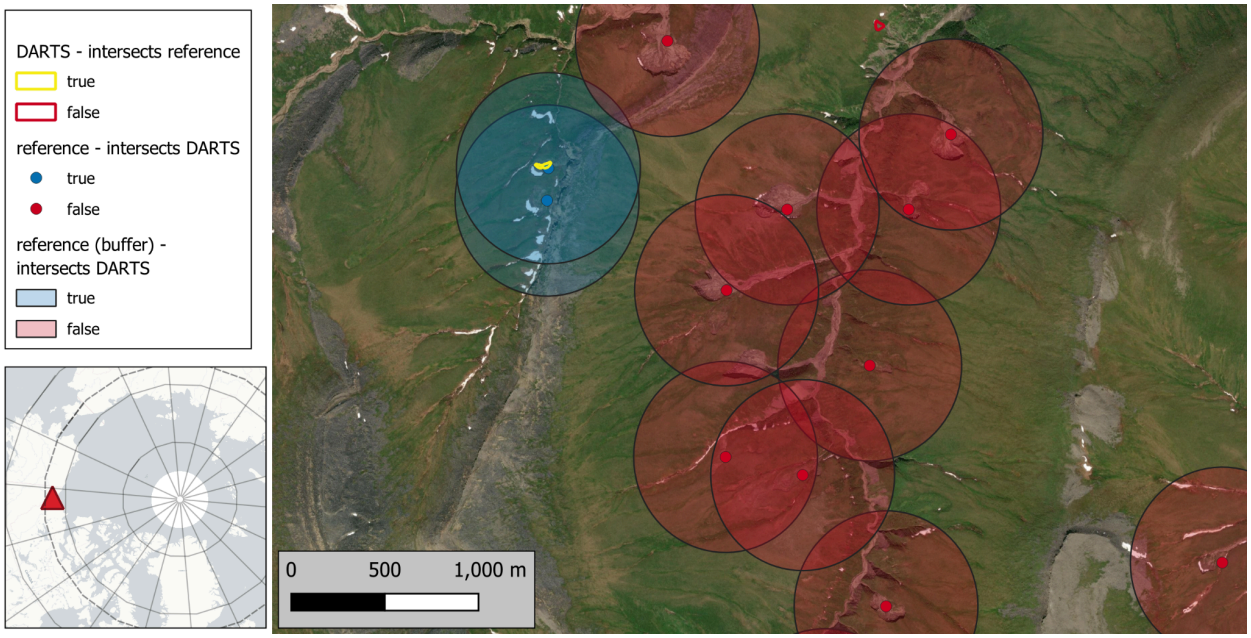

Supplementary Figure S5: Validation of DARTS dataset with the Lewkowicz et al, 2024 reference dataset on the Peel Plateau (68.01 °N, 135.71 °W). DARTS true positives in yellow and reference true positives in blue (point location + 500m buffer) with mutual intersection. DARTS and reference false positives, where datasets do not intersect, are indicated in red. Background Map: *ESRI Satellite*.

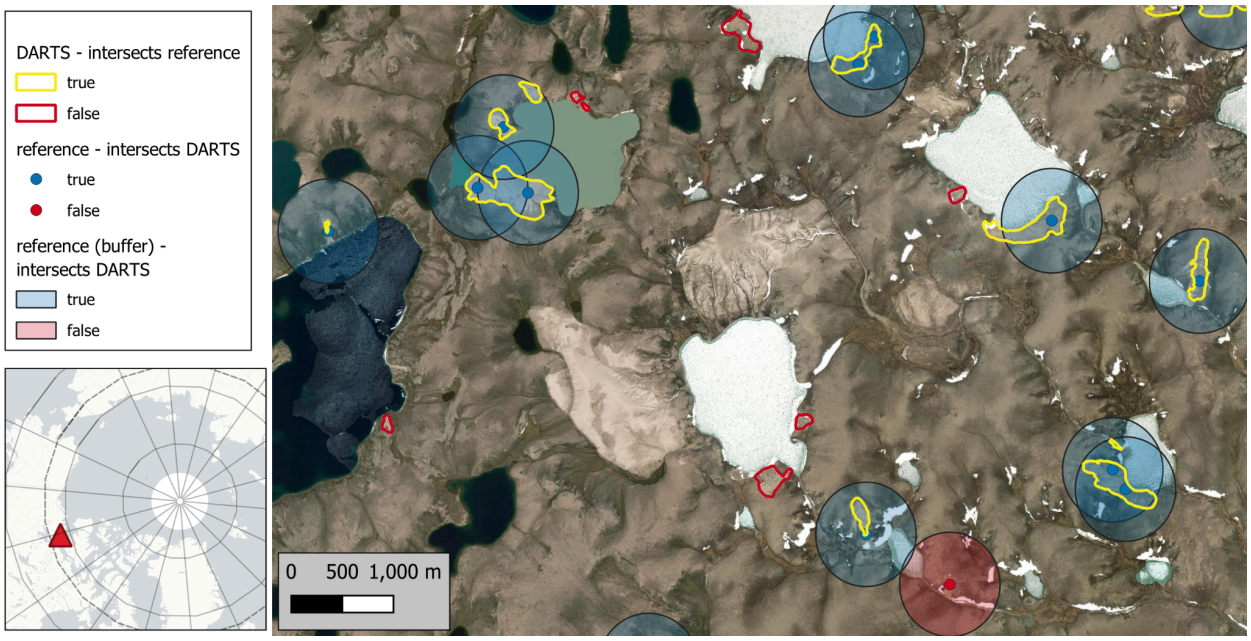

Supplementary Figure S6: Validation of DARTS dataset with the Lewkowicz et al, 2024 reference dataset in the Bluenose Moraine region (68.57 °N, 119.20 °W). DARTS true positives in yellow and reference true positives in blue (point location + 500m buffer) with mutual intersection. DARTS and reference false positives, where datasets do not intersect, are indicated in red. Background Map: *ESRI Satellite*.